

Biodegradable oxygen-evolving metalloantibiotics for spatiotemporal sono-metalloimmunotherapy against orthopaedic biofilm infections

Received: 6 March 2024

Accepted: 10 September 2024

Published online: 14 September 2024

 Check for updates

Zheng Su^{1,6} , Dongdong Xu^{2,6}, Xianli Hu^{1,6}, Wanbo Zhu³ , Lingtong Kong⁴, Zhengzheng Qian⁵, Jiawei Mei¹, Ruixiang Ma¹, Xifu Shang¹, Wenpei Fan⁵  & Chen Zhu¹ 

Pathogen-host competition for manganese and intricate immunostimulatory pathways severely attenuates the efficacy of antibacterial immunotherapy against biofilm infections associated with orthopaedic implants. Herein, we introduce a spatiotemporal sono-metalloimmunotherapy (SMIT) strategy aimed at efficient biofilm ablation by custom design of ingenious biomimetic metal-organic framework (PCN-224)-coated MnO₂-hydrangea nanoparticles (MnPM) as a metalloantibiotic. Upon reaching the acidic H₂O₂-enriched biofilm microenvironment, MnPM can convert abundant H₂O₂ into oxygen, which is conducive to significantly enhancing the efficacy of ultrasound (US)-triggered sonodynamic therapy (SDT), thereby exposing bacteria-associated antigens (BAAs). Moreover, MnPM disrupts bacterial homeostasis, further killing more bacteria. Then, the Mn ions released from the degraded MnO₂ can recharge immune cells to enhance the cGAS-STING signaling pathway sensing of BAAs, further boosting the immune response and suppressing biofilm growth via biofilm-specific T cell responses. Following US withdrawal, the sustained oxygenation promotes the survival and migration of fibroblasts, stimulates the expression of angiogenic growth factors and angiogenesis, and neutralizes excessive inflammation. Our findings highlight that MnPM may act as an immune costimulatory metalloantibiotic to regulate the cGAS-STING signaling pathway, presenting a promising alternative to antibiotics for orthopaedic biofilm infection treatment and pro-tissue repair.

Orthopaedic implant-associated biofilm infections caused by multidrug-resistant bacteria have emerged as an intractable clinical challenge owing to their high risk of recurrence and drug resistance evolution^{1–5}. Implant-adherent bacteria, such as *Escherichia coli* (*E. coli*) and methicillin-resistant *Staphylococcus aureus* (MRSA), which reside in

biofilms, are highly resistant to antibiotics and host immune defenses, resulting in persistent biofilm infections that have a negative impact on public health and the global economy^{6,7}. There is a growing concern about an alternative to traditional surgery and antibiotics that may more easily achieve better therapeutic outcomes⁸. Immunotherapy has

A full list of affiliations appears at the end of the paper. ✉ e-mail: suz924@ustc.edu.cn; zhuwanbo@sjtu.edu.cn; wenpei.fan@cpu.edu.cn; zhuchena@ustc.edu.cn

remarkably revolutionized disease treatment and gained extensive attention. As for innate immune cells, such as neutrophils and macrophages, immunotherapy usually produces unsatisfactory antibiofilm effects due to the lack of immunogenicity and insufficient immune response rate^{9–11}. Even worse, mature bacterial biofilms can conceal antigen presentation to avoid immunosurveillance and subsequent elimination, which is characterized by a low frequency of bacteria-associated antigen (BAA) exposure, an immunosuppressive network in the biofilm microenvironment (BME), and even antigen-presenting cell (APC) killing^{12,13}. Considering the important role of immunostimulatory adjuvants in potentiating infection treatments to synergistically suppress biofilm progression, it is extremely desirable to develop immunological adjuvants with both bactericidal and immunostimulatory effects to both the innate and adaptive immune systems.

Metalloantibiotics, as metal-organic complexes, have garnered increasing attention in recent years due to their unique antimicrobial activity¹⁴ and potential for metalloimmunotherapy^{15,16}. As vital trace elements within biological systems, including bacterial pathogens, metal ions (e.g., Cu²⁺, Zn²⁺, Fe²⁺, Mn²⁺, Ca²⁺, Co²⁺, etc.) can be neither biochemically synthesized nor degraded. Once the metal homeostasis becomes dysfunctional, the bacterial health will be affected. Therefore, regulating metal homeostasis in bacteria presents a promising antibacterial strategy^{17,18}. For instance, when the bacterial Zn²⁺ efflux pump is deleted, the bacteria become more sensitive to Zn²⁺ and are more easily killed by neutrophils¹⁹. Additionally, Fe²⁺-induced ferroptosis-like death in bacteria is developing into an efficacious antibacterial strategy via homeostasis disturbance^{20,21}. Notably, invading pathogens increase the cellular demand for manganese, a nutrient that belongs to the host as a defense against invading pathogens²². New findings indicate that Mn elements acts as a key micronutrient that contributes to the pathogenesis of a variety of bacterial species²³. When the gene encoding the Mn efflux pump (MntE) in the family of cation diffusion facilitator proteins is deleted, *Streptococcus pyogenes* is more readily killed by human neutrophils in vitro²⁴. Moreover, metal ions can also act in immunomodulation²⁵, such as pathogen-host interactions^{26,27} and cGAS-STING (cyclic guanosine monophosphate-adenosine monophosphate synthase-stimulator of interferon genes) signaling^{28,29}. cGAS-STING in APCs is crucial for the coordination of innate immune sensing and subsequent activation of adaptive immune surveillance³⁰. Recent studies have also shown that Mn ions can sensitize the cGAS-STING pathway to double-stranded DNA and synergize with immune checkpoint inhibitors³¹, radiotherapy^{32,33}, adjuvants⁹, in situ vaccines^{34,35}, and photodynamic therapy (PDT)³⁶. Undoubtedly, the equilibrium of STING activation is equally significant³⁷. However, how to systemically develop an effective metalloimmunotherapy and then convert it into appropriate metalloantibiotic forms for BAA-associated immunogenicity enhancement and metal homeostasis modulation, remains largely unknown.

As a representative of porous materials, metal-organic frameworks (MOFs) have been recognized as excellent drug carriers and encapsulation shells for biomedical applications^{38–41}. Among the emerging types of MOFs, porphyrinic MOFs are built from metal ions and heme-like organic ligands⁴². Particularly, porphyrinic MOFs can generate highly cytotoxic reactive oxygen species (ROS) upon ultrasound (US) exposure through a sonodynamic process^{43–45}. Moreover, as an artificial nanozyme, porphyrinic MOFs can catalyze the polymerization of various monomers under a broad range of wavelengths⁴⁶. Recently, porphyrin MOFs have also been applied for encapsulation of small molecule drugs⁴⁷, enzymes⁴⁸, and even nanoparticles⁴⁹ to develop MOF heterostructures with novel additional capacities. For instance, Hu et al.⁵⁰ prepared porphyrinic MOF-based drug nanocarriers for synergetic PDT and chemotherapy. Shao et al.⁵¹ designed a core-shell upconversion nanoparticle@porphyrinic MOF for NIR-induced PDT and tirapazamine-mediated

chemotherapy. Zhang et al.⁴³ pointed out that porphyrinic MOFs were sonosensitizer-integrated backbones for SDT under US exposure. In addition, MOF-encapsulated Mn ions (e.g., Mn₃O₄, Mn₂O₃, MnO₂, MnO, etc.) can avoid normal tissue engulfment and excess dosage-induced systemic toxicity⁵². Collectively, MOF-based metalloantibiotics composed of porphyrinic MOFs and bioactive metal elements, have great potential in bactericidal and BAA-related exposure for metalloimmunotherapy to generate humoral and cellular immune responses.

Here, we develop an innovative spatiotemporal sono-metalloimmunotherapy strategy named “SMIT” against orthopaedic implant-associated biofilm infections by the custom design of porphyrinic MOF-based metalloantibiotics (Fig. 1). Briefly, an Ostwald ripening method is introduced for encapsulation of porphyrinic MOF (porous coordination network-224, PCN-224 or PCN) on a single MnO₂-hydrangea nanoparticle (MnO₂@PCN, MnP). After decoration by hybrid neutrophil/macrophage membranes via biomimetic technology, these porphyrinic MOF-based heterostructured nanoparticles (MnO₂@PCN@Mem, MnPM) will exhibit stimuli-homing responsiveness and inflammatory chemotaxis. Firstly, MnPM can catalyze hydrogen peroxide (H₂O₂) inside the BME into oxygen. Secondly, the generated oxygen can boost oxygen-dependent SDT to kill bacteria via bacterial homeostasis disturbance (e.g., Mn ion overabundance, oxidative stress malfunction, cell membrane integrity deficiency, quorum sensing (QS) system disorder, etc.). Thirdly, the fragments of damaged bacteria as the exposed BAAs escape from the biofilm and are recognized and engulfed by APCs (e.g., macrophages and dendritic cells (DCs), etc.). Meanwhile, the Mn ion-enhanced cGAS-STING pathway activation promotes M1-phenotype macrophage polarization and DC maturation, characterized by the secretion of type-I interferons (IFN-I) and proinflammatory cytokines, to reverse the immunosuppressive state. This augmented APC priming and antigen presentation, activating biofilm-specific T cell responses (CD4⁺, Th17) to suppress biofilms. Of note, oxygen will not be consumed by SDT when US exposure is removed. The sustained oxygen generation can improve the survival and migration of fibroblasts as well as promote the expression of angiogenic growth factors and angiogenesis with elevated secretion of anti-inflammatory factors. Finally, excessive cGAS-STING/Th17-driven inflammation can be neutralized. Overall, MnPM, a metalloantibiotic composed of a sonosensitizer, a nanozyme, and bioactive metal ions, is a prospective alternative to conventional antibiotics and shed light on spatiotemporal antibiofilm sono-metalloimmunotherapy and tissue repair by regulating the cGAS-STING signaling pathway.

Results and discussion

Synthesis and characterization of hydrangea-structured MnO₂ nanoparticles

Hydrangea-structured MnO₂ (MnO₂-hydrangea) nanoparticles were synthesized using a facile “one-pot wet” method by formamide-mediated reduction of potassium permanganate at room temperature. The collected MnO₂-hydrangea nanoparticles showed a hydrangea-like morphology with a rough surface (Fig. 2a and Supplementary Fig. 1), which promoted efficient nano-bio interactions and lead to cellular uptake^{53,54}. The results of Fourier transform near infrared (FTIR) spectra, Ultraviolet-Visible (UV-Vis), and X-ray diffraction (XRD) patterns further confirmed the successful preparation of MnO₂-hydrangea nanoparticles. As shown in Supplementary Fig. 2, FTIR characteristic absorption peaks at 1383, 1641, 2850, and 2923 cm⁻¹ revealed the formation of MnO₂-hydrangea nanoparticles⁵⁵. In Supplementary Fig. 3, a broad UV-Vis characteristic absorption band at around 350 nm was observed due to the surface plasmon of colloidal manganese dioxide⁵⁶. The XRD pattern of MnO₂-hydrangea nanoparticles corresponded well with standard pattern of MnO₂

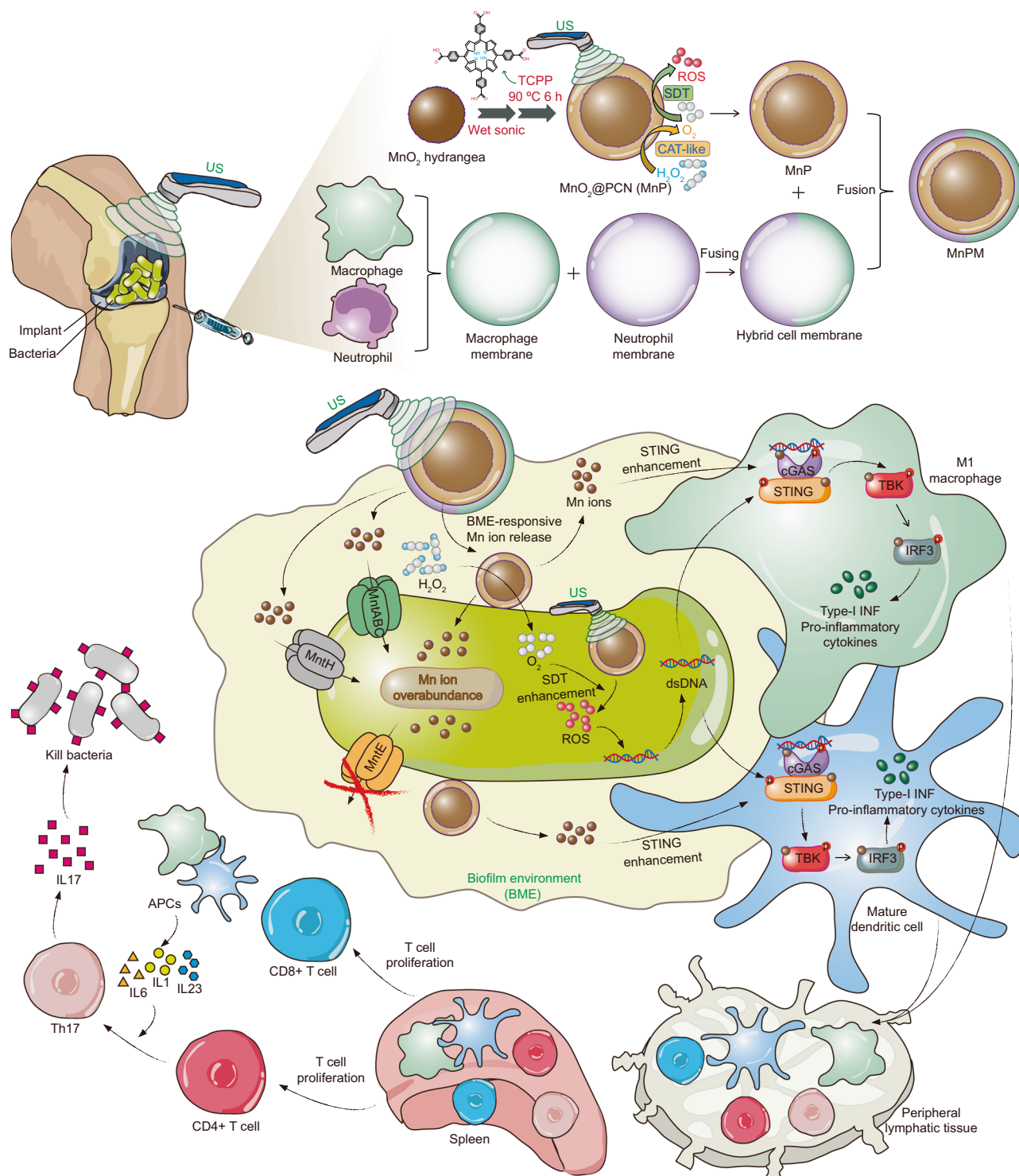


Fig. 1 | Scheme illustrating the mechanism by which MnPM enhances SDT and boosts antibiofilm metalloimmunotherapy. A spatiotemporal SMIT strategy is proposed for biofilm ablation. Upon injection at the biofilm, MnPM can act as an oxygen self-supplying sonosensitizer, thereby enhancing SDT against recalcitrant implant-related infections. Concurrently, the released Mn ions can sensitize the biofilm to SDT by disrupting intracellular homeostasis, further facilitating biofilm degradation. The innate immune system serves as the primary source of

crucial signals required to instigate adaptive immune responses. Consequently, we anticipate these two elements to exhibit significant synergy. Moreover, bacterial fragments (e.g., double-stranded DNA, dsDNA, etc.) as BAAs released from the damaged biofilm can collaborate with Mn ions to initiate effective innate and adaptive antibiofilm immune responses by activating STING to suppress biofilm growth.

(Supplementary Fig. 4). Considering the narrow particle size distribution within the range of 50.73 ± 7.00 nm (Fig. 2b), MnO₂-hydrangea nanoparticles were found to be efficiently taken up by APCs⁵⁷. Importantly, MnO₂-hydrangea nanoparticles with a large surface area

(104.77 m²/g) were able to be used as the cornerstone to construct the core-shell structure (Supplementary Fig. 5). Then, dissolved oxygen experiments were performed to evaluate the catalase-like activity of MnO₂-hydrangea nanoparticles by decomposing H₂O₂ into

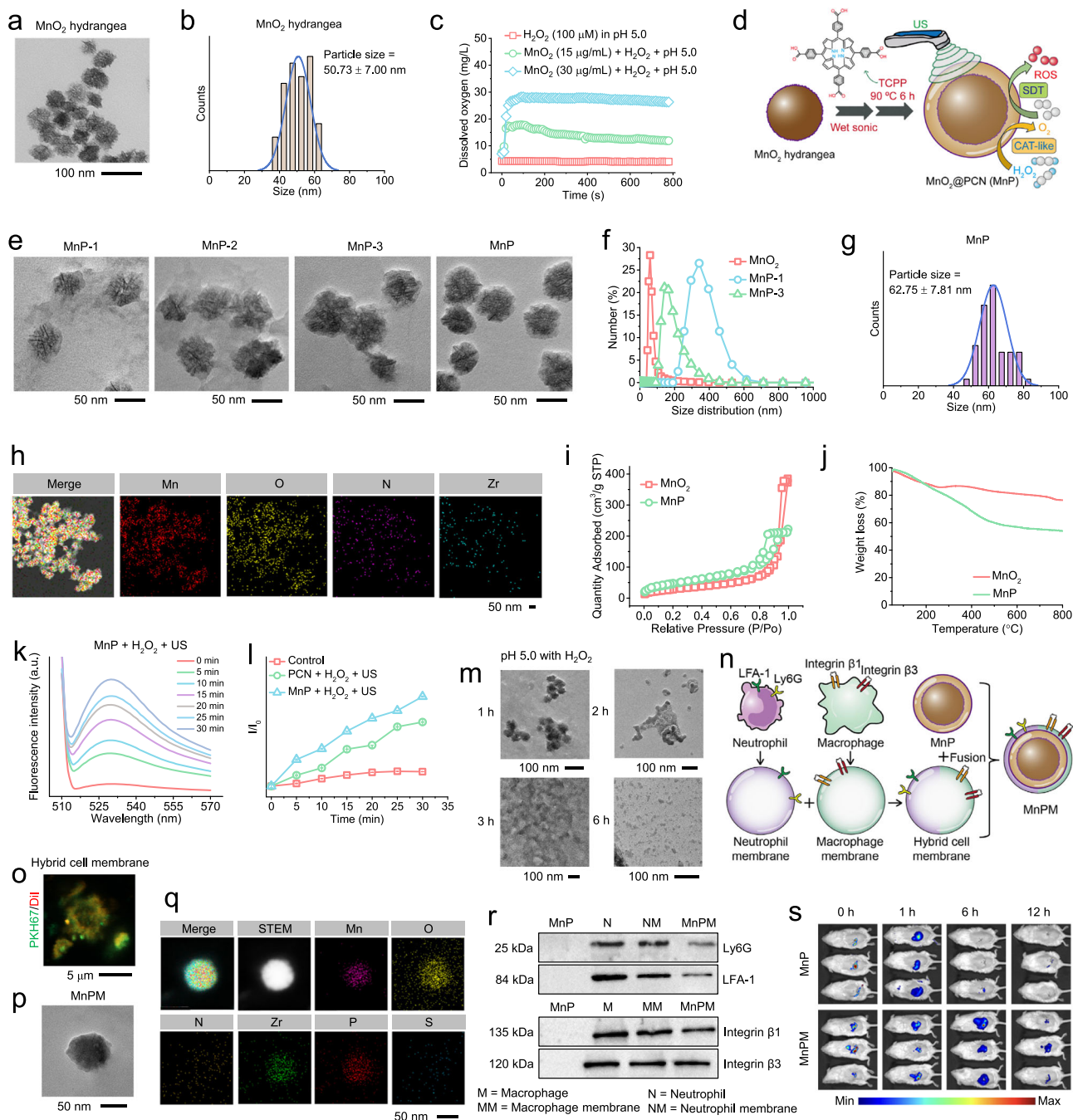


Fig. 2 | Preparation and characterization of MnPM. **a** TEM image of MnO_2 -hydrangea nanoparticles. Scale bar, 100 nm. **b** Particle size distribution of MnO_2 -hydrangea nanoparticles. **c** The effect of H_2O_2 (100 μM) and concentration of MnO_2 nanoparticles on oxygen production. **d** Schematic illustration of the fabrication of MnP for oxygen-enhanced SDT. **e** TEM images of MnP-1, MnP-2, MnP-3, and MnP nanoparticles. Scale bar, 50 nm. **f** Hydrodynamic particle size distribution of MnO_2 , MnP-1, and MnP-3 by DLS. **g** Particle size distribution of MnP. **h** Merged image of MnP nanoparticles with elemental mapping of Mn, O, N, and Zr. Scale bar, 50 nm. **i** N_2 -adsorption-desorption isotherms of MnO_2 and MnP nanoparticles. **j** TGA analysis curves of MnO_2 and MnP nanoparticles. **k** The fluorescence emission spectra of the SOSG assay of the MnP + H_2O_2 + US group for singlet oxygen detection. **l** ROS generation of Control, PCN, and MnP (200 $\mu\text{g}/\text{mL}$) treated with or without 100 μM

H_2O_2 upon US exposure (2 W/cm^2 , 1 MHz, 50%) for 30 min. $n = 3$ independent experiments; means \pm SDs. **m** TEM images of the MnO_2 degradation process at pH 5.0 with H_2O_2 . Scale bar, 100 nm. **n** Schematic illustration of the construction of MnPM. **o** Fluorescence imaging of hybrid membranes of neutrophils and macrophages (green, neutrophil membrane, PKH67; red, macrophage membrane, Dil). Scale bar, 5 μm . **p** TEM image of MnPM nanoparticles. Scale bar, 50 nm. **q** HAADF-STEM image and element-mapping images of MnPM nanoparticles. **r** Western blot analysis of total membrane proteins of MnP, neutrophils, macrophages, neutrophil membranes, macrophage membranes, and MnPM. **s** Biodistribution of Cy5.5-labeled MnP and MnPM in implant-associated biofilm infection mice at 0, 1, 6, and 12 h via *in vivo* bioluminescence imaging. Source data are provided as a Source Data file.

oxygen (Fig. 2c). High dissolved oxygen levels and stable plateau were observed in H_2O_2 -enriched and acidic environments with visible abundant bubbles (Supplementary Fig. 6), suggesting the promising oxygen supply capability of MnO_2 -hydrangea nanoparticles.

Synthesis and characterization of MnP

To endow porphyrinic MOF (PCN-224 or PCN) with enhanced SDT features, an Ostwald ripening method was employed for encapsulation of PCN-224 on a single MnO_2 -hydrangea nanoparticle to synthesize MnP

nanoparticles (Fig. 2d). By varying the feeding concentration of zirconium chloride ($ZrCl_4$) and tetrakis(4-carboxyphenyl)porphyrin (TCPP) while maintaining the same feeding concentration of MnO_2 -hydrangea nanoparticles at 0.583 mg/mL, various types of MnP with different morphologies were synthesized in N,N-dimethylformamide/ethanol (DMF/EtOH) solution (Fig. 2e and Supplementary Fig. 7). The PCN-224 shell failed to adequately cover MnO_2 -hydrangea nanoparticles with a low mass ratio of $ZrCl_4$ /TCPP/ MnO_2 (Supplementary Fig. 8). Compared with MnP, an increased mass ratio of $ZrCl_4$ /TCPP/ MnO_2 resulted in multi-aggregation of MnO_2 -hydrangea nanoparticles (Fig. 2e, MnP-2 and MnP-3) and even homogeneous nucleation of PCN-224 (Fig. 2e, MnP-1). Increased hydrodynamic particle size by dynamic light scattering (DLS) measurement further confirmed the aggregation of MnP-1 and MnP-3 (Fig. 2f). In contrast, MnP, with a particle size distribution centered at 62.75 ± 7.81 nm, exhibited optimized uniform morphology (Fig. 2g). The change in the zeta potentials of various MnPs indicated successful MOF decoration on MnO_2 -hydrangea nanoparticles (Supplementary Fig. 9). The volume ratio of DMF/EtOH also exerted a dramatic impact on the morphology of MnP nanoparticles (Supplementary Fig. 10). The Mn and Zr of MnP were detected by X-ray photoelectron spectroscopy (XPS), as shown in Supplementary Fig. 11. Binding-energy peaks of $Mn2p_{1/2}$ and $Mn2p_{3/2}$ were observed at 653.7 and 641.8 eV, respectively, which were typical values for Mn(IV), suggesting the formation of MnO_2 -hydrangea nanoparticles⁵⁸. Elemental mapping and X-ray energy-dispersive spectroscopy (EDS) spectra revealed the uniform distribution of Zr ions on the surface of MnO_2 -hydrangea nanoparticles, providing additional support for the successful encapsulation of PCN-224 on MnO_2 -hydrangea nanoparticles (Fig. 2h and Supplementary Fig. 12).

After decoration of porous PCN-224 on MnO_2 -hydrangea nanoparticles, the resulting MnP obtained a larger surface area (Fig. 2i and Supplementary Figs. 5,13). In the thermogravimetric analysis (TGA) curves, a distinct weight loss step ranging from 200 °C to 400 °C was observed, which was attributed to the PCN-224 shell in MnP (Fig. 2j). Subsequently, the ROS (singlet oxygen, 1O_2) generation from MnP was measured by singlet oxygen sensor green (SOSG), as shown in Fig. 2k and Supplementary Fig. 14. In contrast to the other groups, the MnP + H_2O_2 + US group exhibited distinct fluorescence emission, implying that oxygen enhanced ROS generation (Fig. 2l). Huang et al.⁵⁹ also reported the effective strategy of oxygen-enhanced SDT. The glutathione (GSH) content was detected using the probe 5,5'-dithiobis-(2-nitrobenzoic acid) (DTNB). The characteristic absorbance of DTNB decreased as time proceeded, indicating that GSH was depleted by MnP (Supplementary Fig. 15). The decreased GSH contents increased the survival of ROS and transformed Mn(IV) into Mn(II)³². Apart from oxygen-enhanced SDT, the depletion of reductive substances also improved the efficiency of SDT. In Fig. 2m, the transmission electron microscopy (TEM) images revealed the degradation process of MnO_2 at pH 5.0 with H_2O_2 . Besides, the UV-Vis absorption spectra further confirmed the acidity/ H_2O_2 -triggered MnO_2 degradation due to the vanishing of characteristic absorption peaks (Supplementary Figs. 16 and 17).

Synthesis and characterization of MnPM

Hybrid Neutrophil and macrophage membranes-coated MnP nanoparticles (MnPM) were prepared by serial physical extrusion (Fig. 2n). Two different cell membranes were fused together (Fig. 2o). Two cell membranes coated on a single MnP homogeneously (Supplementary Fig. 18a–c). Upon extrusion, hybrid membranes spontaneously organized on MnP nanoparticles, forming a core-shell structure (Fig. 2p and Supplementary Fig. 18d). Furthermore, the homogeneous distribution of S and P demonstrated the uniform coverage of the hybrid cell membrane on the MnP nanoparticle (Fig. 2q). The mixture of lipids, proteins, and carbohydrates that make up the cell membrane can interact directly with the surrounding environment and play a critical role in cell recognition, signaling, and adhesion⁶⁰. Although the

recruitment of immune cells under the inflammatory conditions described above is complex, recent work has shown that molecules on immune cells play a key role in mediating immune cell recruitment^{61,62}. Therefore, we performed Western blot analysis of the surface molecules on MnP, neutrophils, macrophages, neutrophil membranes, macrophage membranes, and MnPM (Fig. 2r). As markers of neutrophils, lymphocyte function-associated antigen-1 (LFA-1) and lymphocyte antigen 6 complex locus g (Ly6G) were detected on MnPM. Likewise, macrophage-expressed integrin $\beta 1$ and integrin $\beta 3$ were successfully transferred onto the MnPM surface after the cell membrane extrusion process. In addition, more proteins were also successfully transferred onto the MnPM surface via Coomassie brilliant blue staining (Supplementary Fig. 19). To demonstrate the efficient enrichment of MnPM at the site of infection, Cy5.5-labeled MnPM and Cy5.5-labeled MnP were injected into the infected site in the implant-associated biofilm infection mice. Compared with MnP, more MnPM enriched in the infected area and retained there longer (Fig. 2s and Supplementary Fig. 20). Inductively coupled plasma mass spectrometry (ICP-MS) also revealed the larger Mn concentration at the infected area with Cy5.5-labeled MnPM injection (Supplementary Fig. 21). In summary, the well-designed MnPM inherently captured specific protein markers from both neutrophils and macrophages, which contributed to the efficient enrichment of MnPM. MnPM enriched well in both infection-induced and excessive immunity-induced inflammatory microenvironments.

In vitro antibiofilm effect

Antibiofilm is a prerequisite for addressing orthopaedic implant-related infection. Here, we evaluated the potential antibacterial activity of MnP against *E. coli* and MRSA in vitro. As shown in Fig. 3a, noticeable biofilm structural defects were visualized via scanning electron microscopy (SEM) in the PCN + US and MnP + US groups, indicating the efficacious antibiofilm performance of SDT. Three-dimensional reconstructions of the fluorescence-labeled *E. coli* and MRSA biofilms via confocal laser scanning microscopy (CLSM) further verified the oxygen-enhanced SDT in the MnP + US group (Fig. 3b). Visible biofilm detachment was observed. Crystal violet staining revealed that the biofilms maintained structural integrity in the Control, US, PCN, and MnP groups (Fig. 3c). In contrast, after treatment with PCN + US and MnP + US, significant biomass loss of the biofilms was observed (Fig. 3d). The assessment of colony-forming units (CFU) in different groups via the standard plate count method (SPM) revealed an optimal bactericidal effect in the MnP + US group with minimal bacterial colony residue (Fig. 3e, f). Notably, the structural destruction of the biofilm and the death of the bacteria resulted in greater leakage of dsDNA from the bacteria (Fig. 3g). Likewise, flow cytometry scatter plots showed increased propidium iodide (PI)-positive rates, indicating the efficient bactericidal ability of the MnP + US treatment (Fig. 3h–k). The treatment of MnP + US also killed planktonic bacteria (Supplementary Fig. 22). Then, we used Vitamin C (Vc) to scavenge the ROS in MnP + US group, the antibiofilm activity of MnP + US treatment was inhibited (Supplementary Fig. 23). The HAADF-STEM and fluorescence 3D reconstruction revealed the distribution of MnP in bacteria and biofilms, MnP penetrated into the biofilms and attached on the surface of bacteria (Supplementary Fig. 24). Taken together, the reduction in biofilms increased antigen release and allowed better access to antigens by immune cells. Cellular debris from damaged bacteria is an important source of bacterial antigen presentation and can be rapidly internalized by APCs⁶³. Intriguingly, the antibacterial effect of Mn ion in the MnP group was not to be ignored, so further antibiofilm mechanism research was conducted.

In vitro antibiofilm mechanism

To explore the underlying mechanism of MnP + US on MRSA biofilm elimination, RNA sequencing (MnP + US *vs* Control, with three

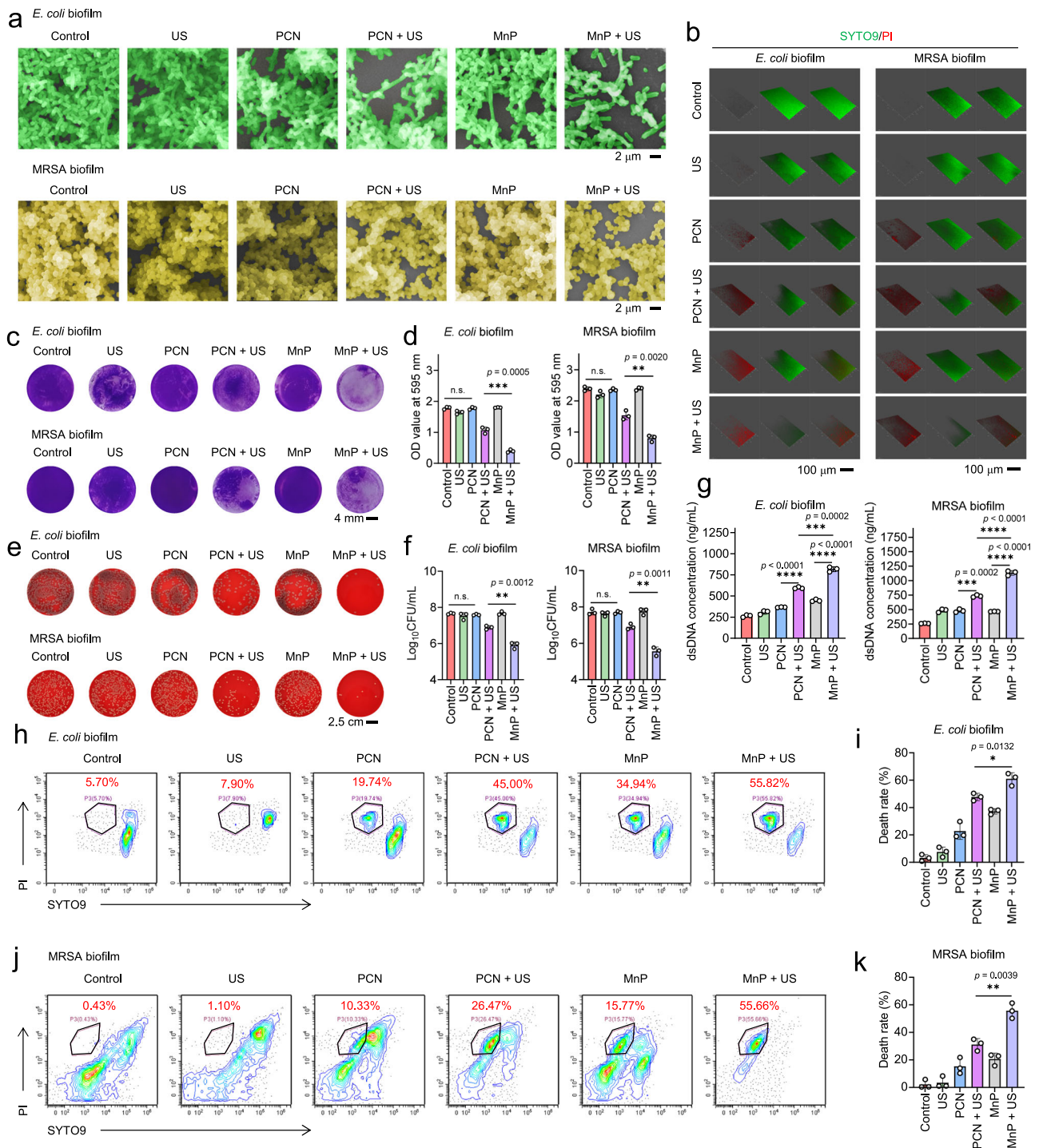


Fig. 3 | In vitro antibiofilm effect. **a** SEM images of *E. coli* and MRSA biofilms treated with Control, US, PCN, PCN + US, MnP, and MnP + US. Scale bar, 2 μ m. **b** Three-dimensional reconstructions of the fluorescence-labeled *E. coli* and MRSA biofilms stained with SYTO9 (green, indicating dead and live bacteria) and PI (red, indicating dead bacteria). Scale bar, 100 μ m. **c** Macroscopic *E. coli* and MRSA biofilm images of the Control, US, PCN, PCN + US, MnP, and MnP + US groups with crystal violet staining. Scale bar, 4 mm. **d** Biofilm biomass of *E. coli* and MRSA biofilms after various treatments. $n = 3$ independent experiments; means \pm SDs. n.s., not significant; * $p < 0.05$, ** $p < 0.01$, *** $p < 0.001$, and **** $p < 0.0001$ using two-tailed Student's t tests. **e** Typical photos of disrupted bacterial colonies from *E. coli* and MRSA biofilms in the Control, US, PCN, PCN + US, MnP, and MnP + US groups.

Scale bar, 2.5 cm. **f** Number of CFUs of *E. coli* and MRSA in six different treatment groups determined by SPM. $n = 3$ independent experiments; means \pm SDs. n.s., not significant; * $p < 0.05$, ** $p < 0.01$, *** $p < 0.001$, and **** $p < 0.0001$ using two-tailed Student's t tests. **g** The dsDNA concentration of *E. coli* and MRSA biofilms in six different treatment groups. $n = 3$ independent experiments; means \pm SDs. n.s., not significant; * $p < 0.05$, ** $p < 0.01$, *** $p < 0.001$, and **** $p < 0.0001$ using two-tailed Student's t tests. Flow cytometry scatter plots of PI and SYTO9 co-staining of *E. coli* (**h**, **i**) and MRSA (**j**, **k**) detached from the biofilms after various treatments with quantitative analysis. $n = 3$ independent experiments; means \pm SDs. n.s., not significant; * $p < 0.05$, ** $p < 0.01$, *** $p < 0.001$, and **** $p < 0.0001$ using two-tailed Student's t tests. Source data are provided as a Source Data file.

replicates) was performed with a total of 1024 differentially expressed genes (526 upregulated and 498 downregulated) (Supplementary Fig. 25). The enrichment analysis of Kyoto Encyclopedia of Gene and Genomes (KEGG) and Gene Ontology (GO) term revealed a series of downregulated pathways after the MnP + US treatment, such as QS, peroxisome, two-component system, ABC transporters, *S. aureus* infection, carotenoid biosynthesis, arginine biosynthesis, fructose and mannose metabolism, amino sugar and nucleotide sugar metabolism, and pyrimidine metabolism (Fig. 4a, b). Taken together, these downregulated differentially expressed genes were largely associated with the QS system, cytosolic membrane integrity, antioxidant proteases, and Mn ion homeostasis. The downregulated genes related to the QS system and bacterial biofilm formation, such as *AgrA*, *AgrB*, and *secA2*, were shown in the MnP + US group (Fig. 4c). Through heat map analysis, cytosolic membrane integrity-related genes were enriched as visible with downregulated expression (Fig. 4d). Antioxidant protease-related genes, including *qoxA*, *qoxD*, and *gpx*, were also downregulated in the MnP + US group (Fig. 4e). Notably, the MnP + US treatment influenced Mn ion homeostasis, such as upregulation of Mn ion uptake genes and downregulation of Mn ion efflux genes, as shown in Fig. 4f.

Interestingly, opposite trends about *AgrA* and *AgrB* were obtained in Fig. 4g. QS system is an important pathway for bacterial adaptation to environmental changes and stress response. Perhaps in the early stage of treatment, the stress response system of bacteria tried to relieve QS system disorder by upregulating *AgrA* and *AgrB*. However, the RNAseq results most likely reflected the later stage of treatment, where the bacterial membrane was completely disrupted and the QS system thoroughly lost the ability of stress response with downregulated *AgrA* and *AgrB*. When we extended the time of the treatment, *AgrA* and *AgrB* decreased significantly as shown in Supplementary Fig. 26. In addition, related transcriptomic results were validated using a BCA leakage assay and an o-nitrophenol- β -D-galactoside (ONPG) assay (Fig. 4h). Downregulation of antioxidant enzyme expression genes indicated the decreased antioxidant capacity of bacteria. Reduced glutathione peroxidase (GPx) and superoxide dismutase (SOD) activities, as well as increased ROS levels, confirmed the imbalanced redox homeostasis and elevated oxidative stress levels (Fig. 4i). After treatment with MnP + US, the bacteria failed to maintain their structural integrity, resulting in the leakage of Mn ions (Fig. 4j). In addition, clear Mn ion overabundance was observed using element mapping analysis (Fig. 4k). The differential gene expression, such as upregulated Mn ion uptake genes (e.g., *MntH*, *MntABC*, etc.) and downregulated Mn ion efflux genes (e.g., *MntE*, etc.), further confirmed the mechanism of Mn ion overabundance, which was a novel type of ion-induced bacterial death involving Mn ions (Fig. 4l,m). Undeniably, there is complexity in the mechanism of bacterial death, but the major bacterial lethal factors, especially overloaded Mn ions, deserve attention.

In vitro promotion of the cGAS-STING pathway

Large amounts of Mn ions released from degraded MnO₂ recharged immune cells (e.g., macrophages, DCs, etc.). To demonstrate the formation of in situ STING activation (Fig. 5a), we first investigated whether MnP was able to effectively activate the cGAS-STING pathway via western blotting (Fig. 5b, c). After treatment with MnP + dsDNA, the APCs (RAW264.7 and DC2.4 cells) exhibited a significant increase in the relative expression of cGAS-STING axis genes and STING-induced inflammatory response genes (Fig. 5d, e and Supplementary Fig. 27). The Mn ions released from MnP effectively activated the STING pathway. Phosphorylation analysis of STING showed that the MnP + dsDNA treatment effectively activated cGAS-STING signal transduction in both RAW264.7 and DC2.4 cells. In addition, through the detection of enzyme-linked immunosorbent assay (ELISA), MnP + dsDNA induced the overexpression of *Ifn-I*, which was a marker of activation of the

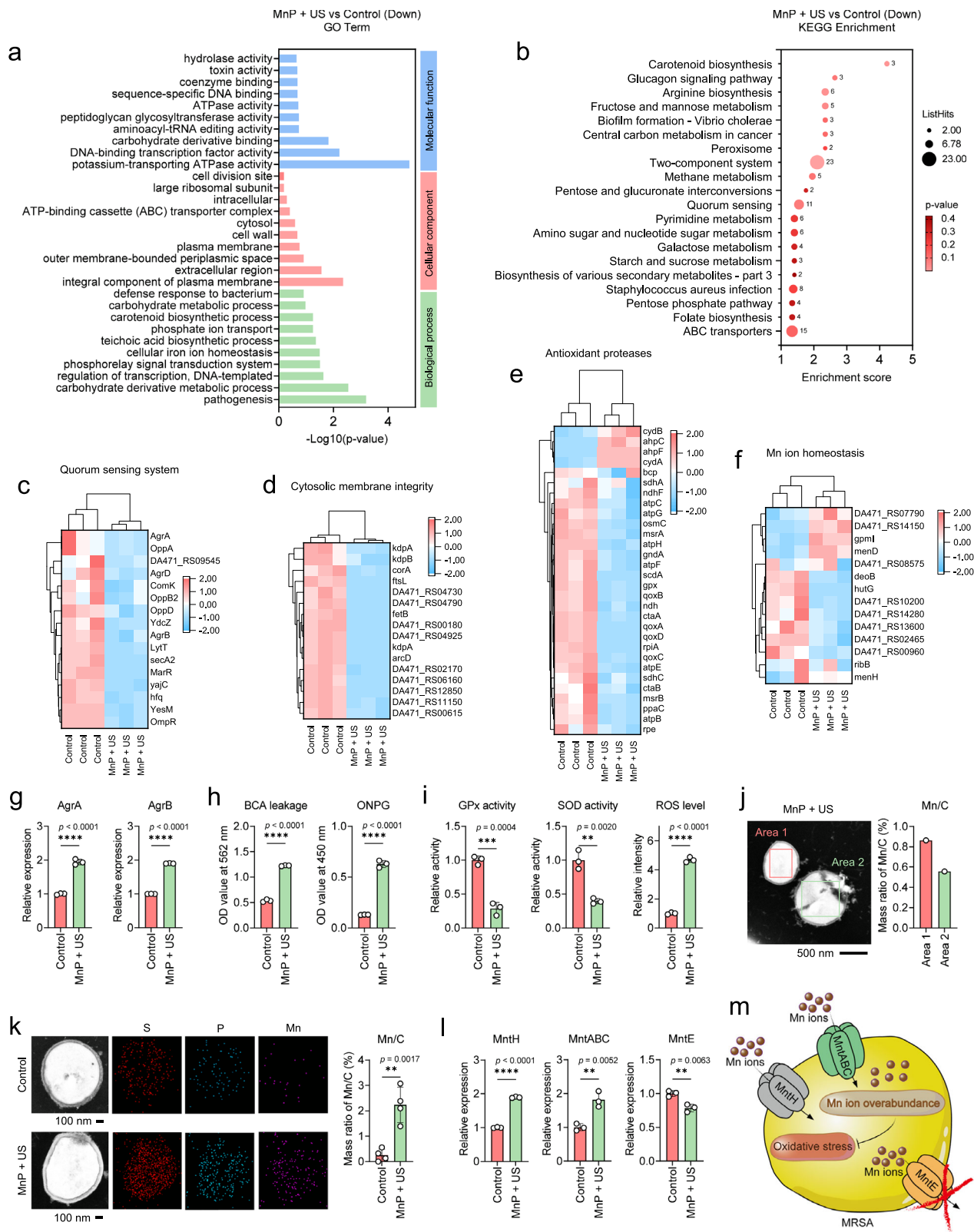
cGAS-STING signaling pathway (Fig. 5f and Supplementary Fig. 28). Furthermore, the DC maturation rate reached 47.86% after treatment with MnP + dsDNA, compared to 37.11% in the PCN + dsDNA group (Fig. 5g). Consistent with the STING signaling activation results, the dsDNA and PCN + dsDNA groups also promoted DC differentiation due to the bacterial antigens (Fig. 5h). Herein, compared to the groups without Mn ions, the release of Mn ions from MnP into DCs promoted both STING activation and DC maturation with significantly increased efficiency (Fig. 5i, j). Release of bacterial antigens was associated with enhanced STING signaling activation and subsequent presentation of APCs, which further reinforced adaptive antibiofilm immune responses.

In vivo healing of implant-associated biofilm infections

Encouraged by the in vitro antibiofilm and immunostimulatory abilities of the SMIT strategy, we established an implant-associated biofilm infection mouse model and tried to evaluate the in vivo antibiofilm effect of the SMIT strategy (Fig. 6a). The administration of MnPM + US significantly suppressed the infection process compared to other treatments (Fig. 6b). Infection-induced subcutaneous abscesses and skin defects were visualized in the Control group even on day 14. According to the bacterial SPM analysis, the MnPM + US treatment damaged biofilm infection in both implants and peripheral tissues (Fig. 6c). In addition, the Vancomycin group also showed good antibiofilm ability, but the evolution of bacterial resistance could not be ignored. In the Null Control group, almost no bacteria were found on implant or in peripheral tissue (Supplementary Fig. 29). Almost no bacteria were observed on the implant in the MnPM + US group (Supplementary Fig. 30). Notably, the mice treated with MnPM + US exhibited elevated levels of proinflammatory cytokines and inflammatory chemokines, such as *Il6*, *Tnf α* , *Cxcl9*, *Cxcl10*, and *Ccl2* (Fig. 6d and Supplementary Fig. 31). Immune characterization of spleens and peripheral tissues demonstrated that the SMIT strategy activated the antibiofilm immune response (Fig. 6e-j). The gating strategies used for in vivo flow cytometric analysis of immune cell populations were shown in Supplementary Fig. 32. The MnPM + US treatment promoted the maturation of DCs and elevated the levels of CD4 + T cells and M1 macrophages. The biofilm-induced frustrated and exhausted state of APCs was characterized by the elevated expression of mannose receptor (CD206) on macrophages and the immaturity of DCs. The SMIT strategy facilitated bacterial antigen processing and presentation, as evidenced by the state transitions of APCs. These results clearly presented how the SMIT strategy was able to induce strong antibiofilm immune responses. Given that antibiotics as a clinical strategy for the treatment of biofilm infections are often accompanied by the unfavorable evolution of bacterial resistance, this advanced SMIT strategy is expected to provide an effective alternative to conventional antibiotic therapy for the reversal of immunosuppressive BME.

In vivo transcriptomics analysis

Furthermore, to unveil the potential in vivo ramification mechanism of spatiotemporal SMIT treatment (MnPM + US), the mouse wound infection model was established on BALB/c mouse. 200 μ L MnPM (30 μ g/mL) was injected into the tissue at the wound MRSA infection site on the back of mice. In the MnPM + US group, the US power = 1.5 W/cm², frequency = 1 MHz, duty cycle = 50%, and irradiation time = 8 min. Wound tissues were taken for transcriptomic analysis. We monitored in vivo oxygen generation via a small animal photoacoustic imaging system, which made sure the sustained oxygen generation (Supplementary Fig. 33). Then, transcriptomic analysis was performed to investigate the transcriptional profiles after the SMIT therapeutic strategy in vivo on day 3, with a total of 887 differentially expressed genes ($|\log_2 FC| > 1$ and $q\text{-value} < 0.05$) between the Control and MnPM + US groups (Supplementary Fig. 34a). Bacterial death-triggered dsDNA release stimulated a series of immune system process with



activated signaling pathways (Fig. 7a), such as NOD-like receptor, cytosolic DNA-sensing, and Toll-like receptor pathways (Fig. 7b). The upregulation of the HIF-1 α signaling pathway was attributed to immune cell infiltration and SDT-induced oxygen consumption. Related transcriptomics analysis confirmed the SDT-induced hypoxia shown in Supplementary Fig. 35. The assistance of Mn ions significantly enhanced the activation of STING signaling pathways associated with

IFN-I responses, proinflammatory cytokines, and chemokine expression. Then, STING activation triggered multiple signaling cascades, leading to activation of the NF-kappa B, TNF, and IL17 signaling pathways, as shown by gene set enrichment analysis (GSEA) in Fig. 7c–g. Related genes, such as *Sting1*, *Il17a*, *Il23a*, *Il1b*, *Il6*, *Tbk1*, *Nfkb2*, *Ifnb1*, and *Tnf*, were significantly upregulated in the MnP + US group according to the results from heat map and GO enrichment chord plot

Fig. 4 | In vitro antibiofilm mechanism. Bacterial transcriptomics analysis. GO term (a) and KEGG enrichment (b) analysis of downregulated genes in bacteria between the Control and MnP + US groups. Heat map analysis of differentially expressed genes about QS system (c), cytosolic membrane integrity (d), anti-oxidant proteases (e), Mn ion homeostasis (f) between the Control and MnP + US groups. **g** Relative gene expression of AgrA and AgrB. $n = 3$ independent experiments; means \pm SDs. n.s., not significant; * $p < 0.05$, ** $p < 0.01$, *** $p < 0.001$, and **** $p < 0.0001$ using two-tailed Student's t tests. **h** BCA leakage and ONPG test of MRSA biofilm. $n = 3$ independent experiments; means \pm SDs. n.s., not significant; * $p < 0.05$, ** $p < 0.01$, *** $p < 0.001$, and **** $p < 0.0001$ using two-tailed Student's t tests. **i** Antioxidant capacity evaluation, including GPx activity, SOD activity, and

ROS levels in biofilms. $n = 3$ independent experiments; means \pm SDs. n.s., not significant; * $p < 0.05$, ** $p < 0.01$, *** $p < 0.001$, and **** $p < 0.0001$ using two-tailed Student's t tests. **j** TEM image of MRSA treated by MnP + US with quantitative analysis. Scale bar, 500 nm. **k** Elemental mapping of the Mn ion with quantitative analysis. Scale bar, 100 nm. $n = 3$ independent experiments; means \pm SDs. n.s., not significant; * $p < 0.05$, ** $p < 0.01$, *** $p < 0.001$, and **** $p < 0.0001$ using two-tailed Student's t tests. **l** Relative gene expression of MntH, MntABC, and MntE. $n = 3$ independent experiments; means \pm SDs. n.s., not significant; * $p < 0.05$, ** $p < 0.01$, *** $p < 0.001$, and **** $p < 0.0001$ using two-tailed Student's t tests. **m** Schematic of Mn ion overabundance. Source data are provided as a Source Data file.

(Supplementary Fig. 34b, c). The differentiation of Th17 cells requires the cytokines IL1b and IL6. Proinflammatory cytokines play a crucial role in activating DC maturation and T cell activation. These studies indicated that the MnPM + US treatment effectively broke the biofilm barrier and utilized the biofilm as endogenous BAAs deposition to further activate adaptive antibiofilm immunity.

On day 10, a total of 1939 dramatically differentially expressed genes (948 upregulated and 991 downregulated) with significant ($|\log_2 FC| > 1$ and $q\text{-value} < 0.05$) expression patterns before and after the MnPM + US treatment was identified (Supplementary Fig. 36a). Among them, tissue repair-related genes involved in intermediate filament organization, keratinization, hair follicle development, and epithelial cell differentiation were remarkably upregulated (Fig. 7h). As shown in the KEGG analysis, effective biofilm killing and continued oxygen generation activated tissue repair-related signaling pathways (Fig. 7i), such as DNA replication, cell cycle, ribosome biogenesis in eukaryotes, mismatch repair, and nucleotide excision repair, via GSEA (Fig. 7j–n). Related genes were significantly upregulated after treatment with MnPM + US (Supplementary Fig. 36b, c). Together, these transcriptome profiles demonstrated that the well-developed spatiotemporal SMIT treatment was able to alter the balance of immunosuppressive and coactivating signaling pathways to achieve an antibacterial immune response and promote tissue repair by regulating the cGAS-STING signaling pathway.

In vitro pro-tissue repair evaluation

Excessive cGAS-STING/Th17-driven inflammation is no longer protective but can instead cause severe inflammatory diseases^{64–66}. Hypoxia alters the populations of monocytes and macrophages during infection, which leads to persistent inflammation that hinders tissue repair after infection treatment⁶⁷. Furthermore, long-term hypoxia in wounds impairs the healing process by inhibiting angiogenesis, re-epithelialization, and extracellular matrix synthesis⁶⁸. Once US irradiation was withdrawn, the oxygen generated from MnP would not be converted to 1O_2 by PCN and sustained oxygenation would reshape the immune landscape after the SMIT treatment (Fig. 8a). The released oxygen effectively increased M2-phenotype macrophage polarization in the MnP group (Fig. 8b, c). The qPCR results revealed that pro-inflammatory factors were significantly downregulated due to the oxygen generation from MnP (Fig. 8d and Supplementary Fig. 37). The ELISA results further confirmed the reversal of the proinflammatory microenvironment with upregulated vascular endothelial growth factor (Vegf) (Fig. 8e).

To assess whether the generated oxygen was able to facilitate the migration of human umbilical vein fusion (EA.hy926) cells, a scratch assay was conducted (Fig. 8f). After treatment with MnP, the migration ratio of EA.hy926 cells was clearly increased (Fig. 8g). In the Transwell migration assay, MnP significantly stimulated the mobility of EA.hy926 cells compared to other treatments (Fig. 8h, i). To evaluate the potential of oxygen generation in promoting angiogenesis, EA.hy926 cells were subjected to in vitro vascular tube formation (Fig. 8j). In the MnP group, the EA.hy926 cells assembled with a significantly greater number of circles, exhibited an ~4.8-fold

increase in circle number compared to those in the Control group (Fig. 8k). Following the removal of US, the sustained oxygenation enhanced the migration of fibroblasts and promoted angiogenesis, accompanied by an elevated secretion of anti-inflammatory factors. The generated oxygen worked well to alleviate the inflammatory immune microenvironment following the SMIT treatment, possessing the great potential to promote healing of infection-induced tissue damage.

In vivo healing of infected skin wounds

To determine whether continuous oxygen generation was able to accelerate infection wound healing, different treatments were administered onto full-thickness excisional wounds in MRSA-infected mice (Fig. 9a). Notably, the wound size in the MnPM + US group was substantially smaller than that in the Control and US groups, demonstrating that the MnPM + US treatment promoted wound closure (Fig. 9b and Supplementary Fig. 38). As a naive T cell subpopulation capable of secreting IL17, Th17 cells are important in autoimmunity and anti-infection defense⁶⁹. Immunohistochemical staining revealed STING axis activation with IL17 and IL23r secretion (Fig. 9c, d). We believed that the emergence of Th17 cells during biofilm infection was associated with the MnPM + US treatment.

According to the histomorphological analysis on day 14, the MnPM + US treatment significantly diminished the infiltration of neutrophils (Fig. 9e, f, H&E). Bacteria in tissues were killed efficiently in the MnPM + US group (Fig. 9e, g, Giemsa). Successful killing of MRSA infection in the MnPM + US group increased collagen deposition (Fig. 9e, h, Masson). The different treatments also affected the immune microenvironment. Immunohistochemistry assays demonstrated numerous CD31-positive cells in the MnPM + US group rather than in the other groups (Fig. 9i). Furthermore, the flow cytometric analysis results revealed that a large number of M2 phenotype macrophages infiltrated the tissue in the MnPM + US group on day 14 (Fig. 9j), suggesting that the infection was effectively eliminated while not causing excessive inflammatory response.

To evaluate the rate of reepithelialization, we used cytokeratin 14 (K14) and cytokeratin 19 (K19), two markers for basal keratinocytes and skin stem cells⁷⁰, respectively, to stain tissue sections harvested on days 3, 10, and 14 (Fig. 9k). The K19-containing keratinocytes were found to localize to a region of hair follicles known as the bulge⁷¹. On day 10, in the MnPM + US group, the complete layer of basal keratinocytes (K14+) nearly encapsulated the wounds. Compared to the other treatments, MnPM + US activated higher migration of more skin stem cells (K19+). On day 14, in the Control, US, and PCNM groups, the migration of basal keratinocytes and skin stem cells was still sluggish. As a key cytokine in the STING axis activation program, IL6 was secreted in large quantities in tissues on day 3 after the MnPM + US treatment (Fig. 9l). In the MnPM + US group, from day 3 to day 10, the amelioration of the proinflammatory microenvironment was able to be visualized by upregulated IL10 and downregulated IL6 in the immunofluorescence staining images (Fig. 9m). By contrast, IL10 was barely secreted in the Control and US groups. These results demonstrated that continuous oxygenation effectively accelerated keratinocyte

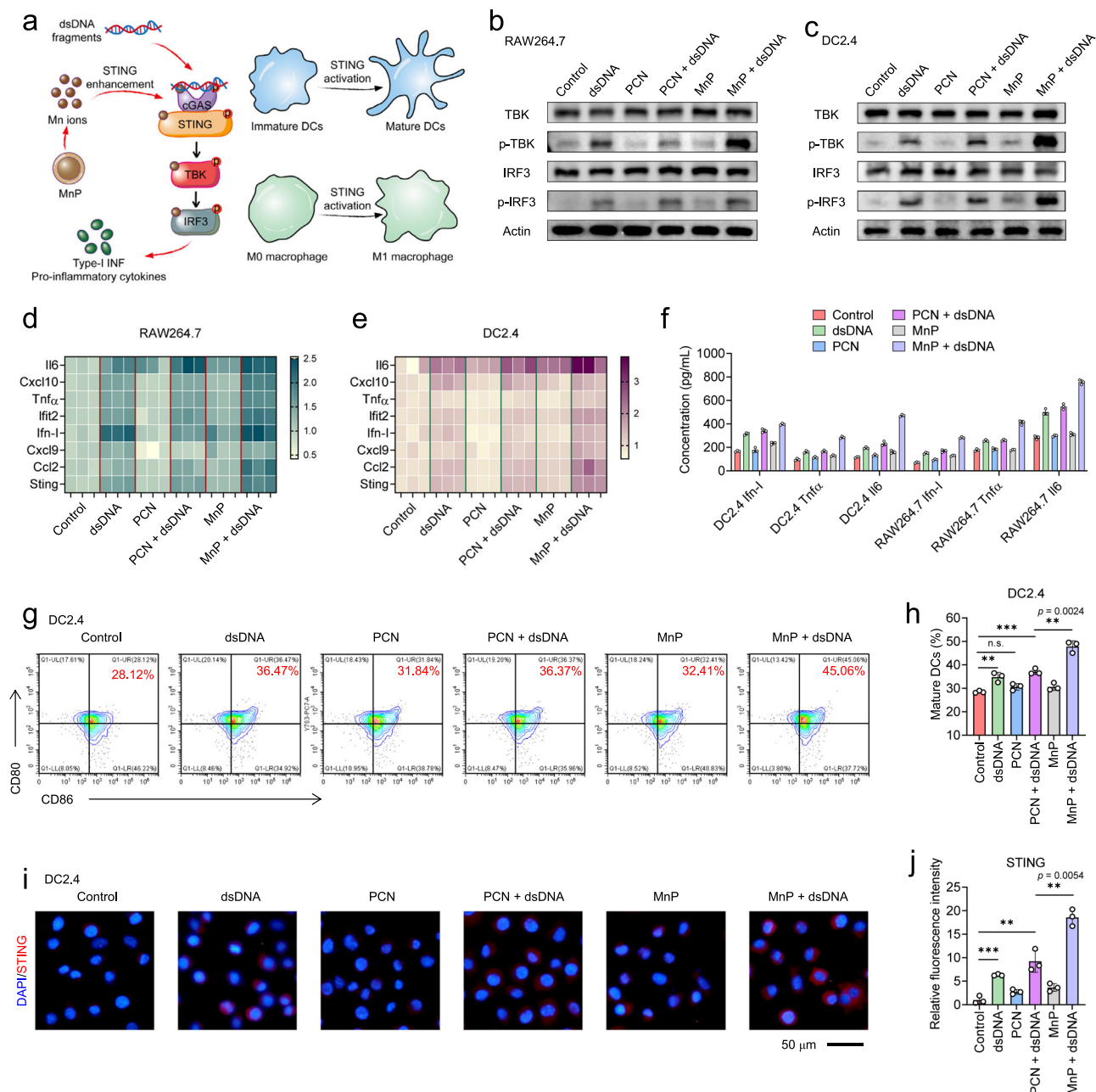


Fig. 5 | In vitro promotion of the cGAS-STING pathway. a Schematic illustration of the promotion of the cGAS-STING pathway. **b, c** Western blot of the activation of the cGAS-STING pathway in APCs (RAW264.7 and DC2.4 cells) after different treatments. Actin = 42 kDa, IRF3 and p-IRF3 = 46 kDa, TBK and p-TBK = 84 kDa. Relative gene expression of the cGAS-STING axis in RAW264.7 (**d**) and DC2.4 (**e**) cells after different treatments by qPCR analysis. **f** ELISA detection of Ifn-1, Tnf α , and Il6 in RAW264.7 and DC2.4 cells after different treatments. **n** = 3 independent experiments; means \pm SDs. n.s., not significant; * p < 0.05, ** p < 0.01, *** p < 0.001, and **** p < 0.0001 using two-tailed Student's t tests. **g** The efficacy of promoting DC

maturation in different groups evaluated by flow cytometry in vitro with quantitative analysis (**h**). n = 3 independent experiments; means \pm SDs. n.s., not significant; * p < 0.05, ** p < 0.01, *** p < 0.001, and **** p < 0.0001 using two-tailed Student's t tests. **i** CLSM images showing STING activation in DCs with quantitative analysis (**j**), where blue represents cell nuclei and red represents STING. Scale bar, 50 μ m. n = 3 independent experiments; means \pm SDs. n.s., not significant; * p < 0.05, ** p < 0.01, *** p < 0.001, and **** p < 0.0001 using two-tailed Student's t tests. Source data are provided as a Source Data file.

migration and hair follicle formation, thereby promoting wound re-epithelialization.

In vitro and in vivo evaluation of biosafety

To confirm the biosafety of the materials, a CCK-8 (cell counting kit-8) assay was used to evaluate the cytotoxic effect in vitro. Accordingly, EA.hy926, RAW264.7, and DC2.4 cells were separately incubated with materials. The relative cell viability remained above 83.7% in the presence of materials (30 μ g/mL), indicating good biocompatibility

(Supplementary Fig. 39). The treatment of MnP + US also did not harm healthy cells (Supplementary Fig. 40). The H&E sections of the kidney, liver, lung, spleen, and heart derived from mice subjected to different treatments exhibited no significant difference, suggesting no obvious tissue toxicity (Supplementary Fig. 41).

In summary, we developed an innovative spatiotemporal SMIT strategy based on custom-designed biomimetic porphyrinic MOF-based metalloantibiotics (MnP) for sono-metalloimmunotherapy against recalcitrant orthopaedic biofilm infections. MnP-induced primary

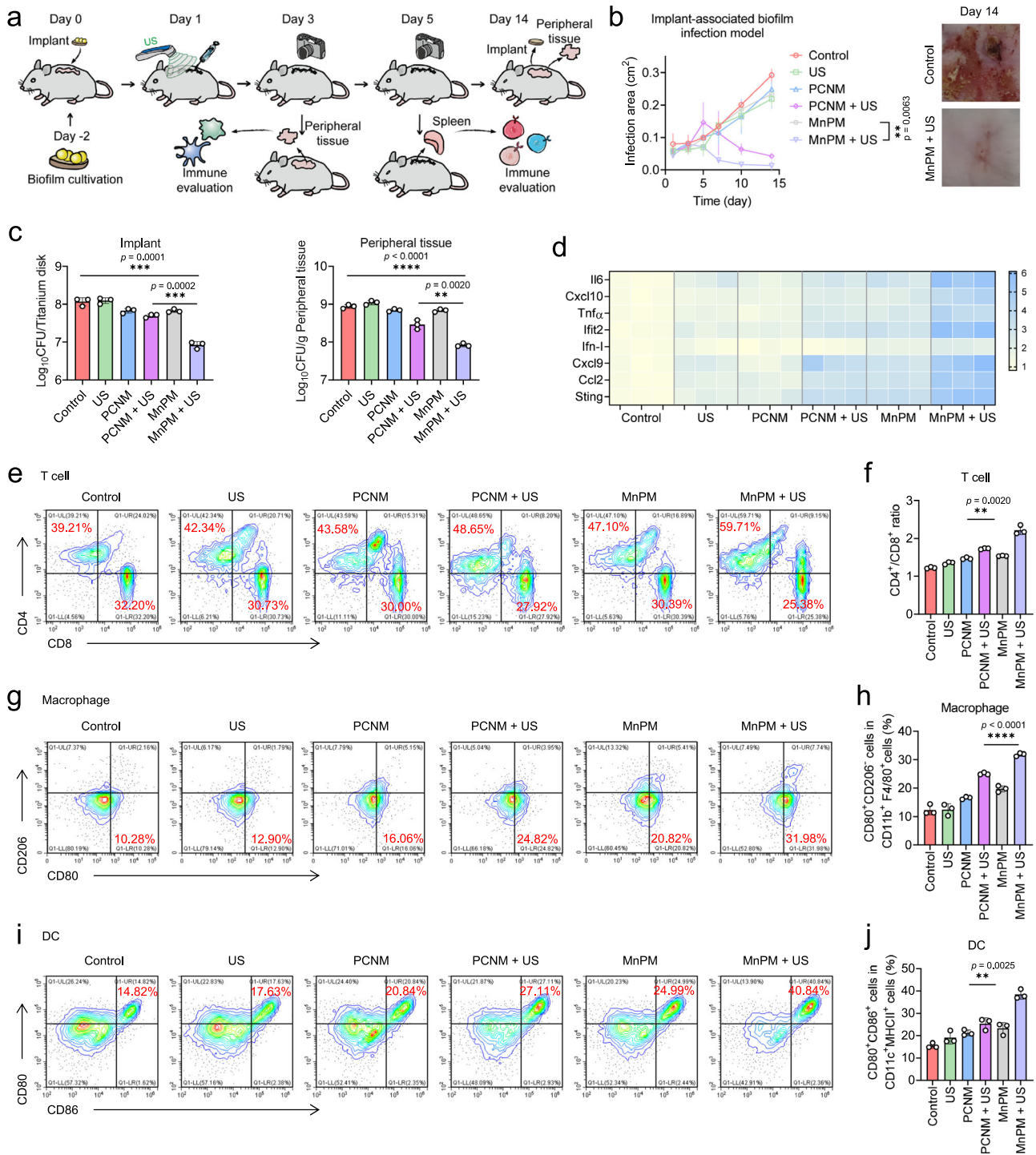


Fig. 6 | Evaluation of the in vivo immunogenic effect in the implant-associated biofilm infection model. **a** Schematic of the implant-associated biofilm infection model and therapeutic procedure of the SMIT strategy. **b** Average infection area change curves in infected mice after different treatments. Representative photos of the Control and MnPM + US groups on day 14. $n = 3$; means \pm SDs; $**p < 0.01$ using Two-way ANOVA. **c** Bacterial CFU counts of residual biofilm on the extracted implants and residual bacteria in the peripheral tissues on day 14. $n = 3$ independent animals; means \pm SDs. n.s., not significant; $*p < 0.05$, $**p < 0.01$, $***p < 0.001$, and $****p < 0.0001$ using two-tailed Student's *t* tests. **d** qPCR analysis of the relative gene expression of the cGAS-STING axis with different treatments. Representative flow cytometry plots of CD4⁺ T cells (CD4⁺) by gating on CD3⁺ T cells (**e**, **f**), M1-phenotype macrophages (CD80 + CD206⁺) by gating on CD11b⁺ + F4/80⁺ cells (**g**, **h**), and mature DCs (CD80 + CD86⁺) by gating on CD11c⁺ + MHC-II⁺ cells (**i**, **j**) in spleens. $n = 3$ independent animals; means \pm SDs. n.s., not significant; $*p < 0.05$, $**p < 0.01$, $***p < 0.001$, and $****p < 0.0001$ using two-tailed Student's *t* tests. Source data are provided as a Source Data file.

bacterial death through SDT and homeostatic disturbances released neo-BAAs, and the combination of Mn ions and BAAs dramatically elevated STING activation in APCs. The intelligent design of MnPM as a metal-antibiotic composed of a sonosensitizer, a nanozyme, and bioactive metal ions enhanced SDT efficiency, amplified T cell responses,

neutralized excessive inflammatory responses, and promoted tissue repair. Moreover, systemic treatments with the spatiotemporal SMIT strategy exerted remarkable biofilm infection elimination efficacy and pro-tissue repair in implant-related biofilm infection models via successful cGAS-STING signaling pathway regulation. Distinct from

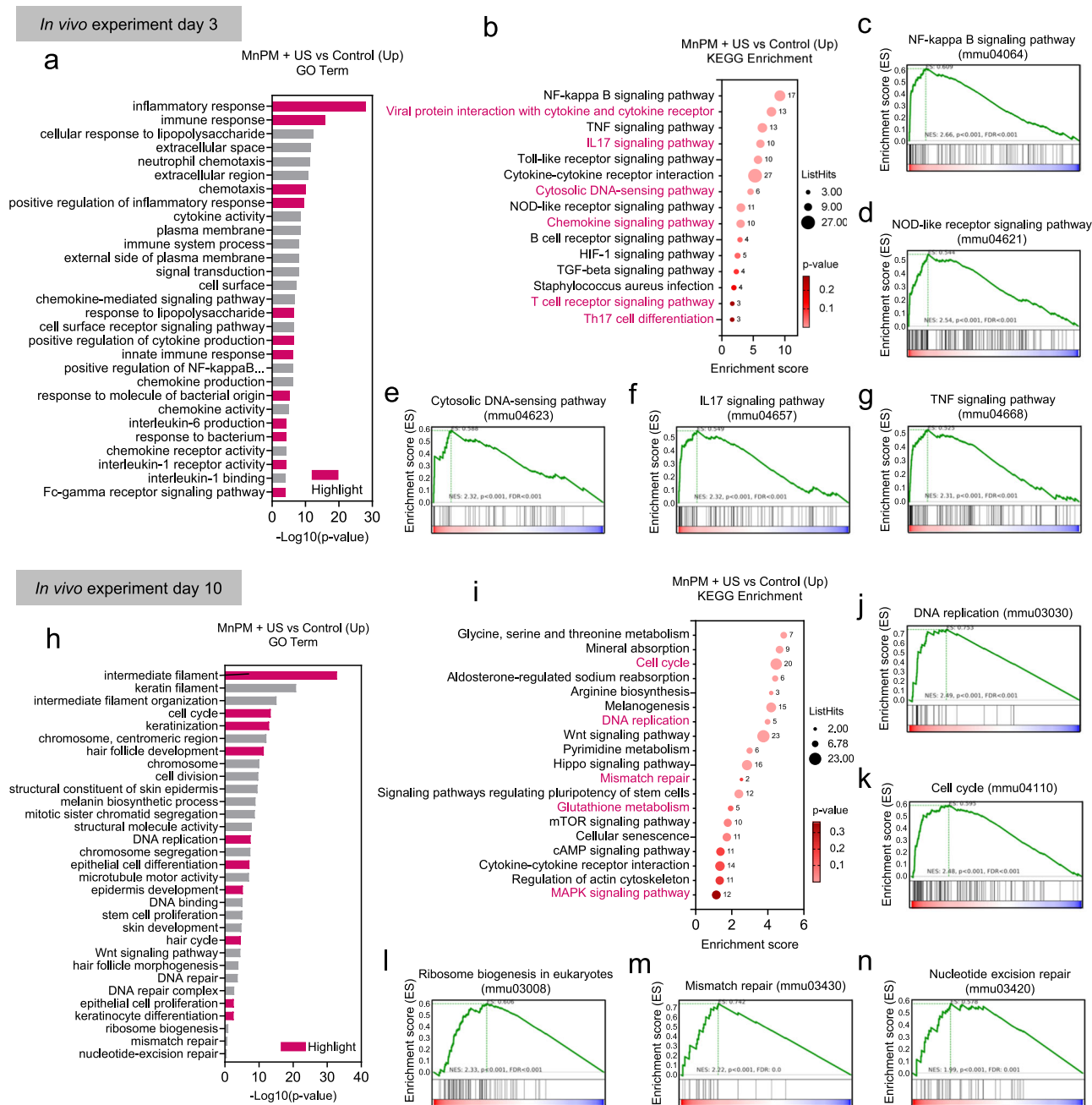


Fig. 7 | In vivo transcriptomics analysis. **a** GO term analysis of upregulated terms after treatment with MnPM + US on day 3. Pink, highlight. **b** KEGG enrichment of upregulated genes after treatment with MnPM + US on day 3. GSEA of representative immune signaling pathways about NF-kappa B (**c**), NOD-like receptor (**d**), cytosolic DNA-sensing (**e**), IL17 (**f**), TNF (**g**) after treatment with MnPM + US on day 3. **h** GO term analysis of upregulated terms after treatment with MnPM + US on day

10. Pink, highlight. **i**, KEGG enrichment of upregulated genes after treatment with MnPM + US on day 10. GSEA of representative repair signaling pathways about DNA replication (**j**), cell cycle (**k**), ribosome biogenesis in eukaryotes (**l**), mismatch repair (**m**), nucleotide excision repair (**n**) after treatment with MnPM + US on day 10. Source data are provided as a Source Data file.

traditional antibiotics, our work presents the concept of metalloantibiotics based on metal-organic framework, demonstrating the tremendous potential of sono-metalloimmunotherapy in killing biofilms, such as dental implant infections, catheter infections, and scaffold infections.

Methods

Mice

All animal experiments were approved by the Animal Ethics Committee of The First Affiliated Hospital of USTC, University of Science and Technology of China Animal Department (2022-N(A)-056). All handling and surgical procedures followed the approved guidelines.

Synthesis and characterization of MnO₂-hydrangea, MnP, and MnPM nanoparticles

The MnO₂-hydrangea nanoparticles were prepared by mixing 950 mg of potassium permanganate (KMnO₄, Aladdin, China) in 480 mL deionized water (DI-water). After stirring for 5 min, 15 mL of formamide (Aladdin, China) was dropped into the above mixed solution, and stirring was continued for 8 h. The final MnO₂-hydrangea products were centrifuged, washed with water, and freeze-dried for further use.

MnP nanoparticles with varying mass ratios of MnO₂ and PCN were prepared by dispersing 140 mg of MnO₂ in 20 mL of a mixed

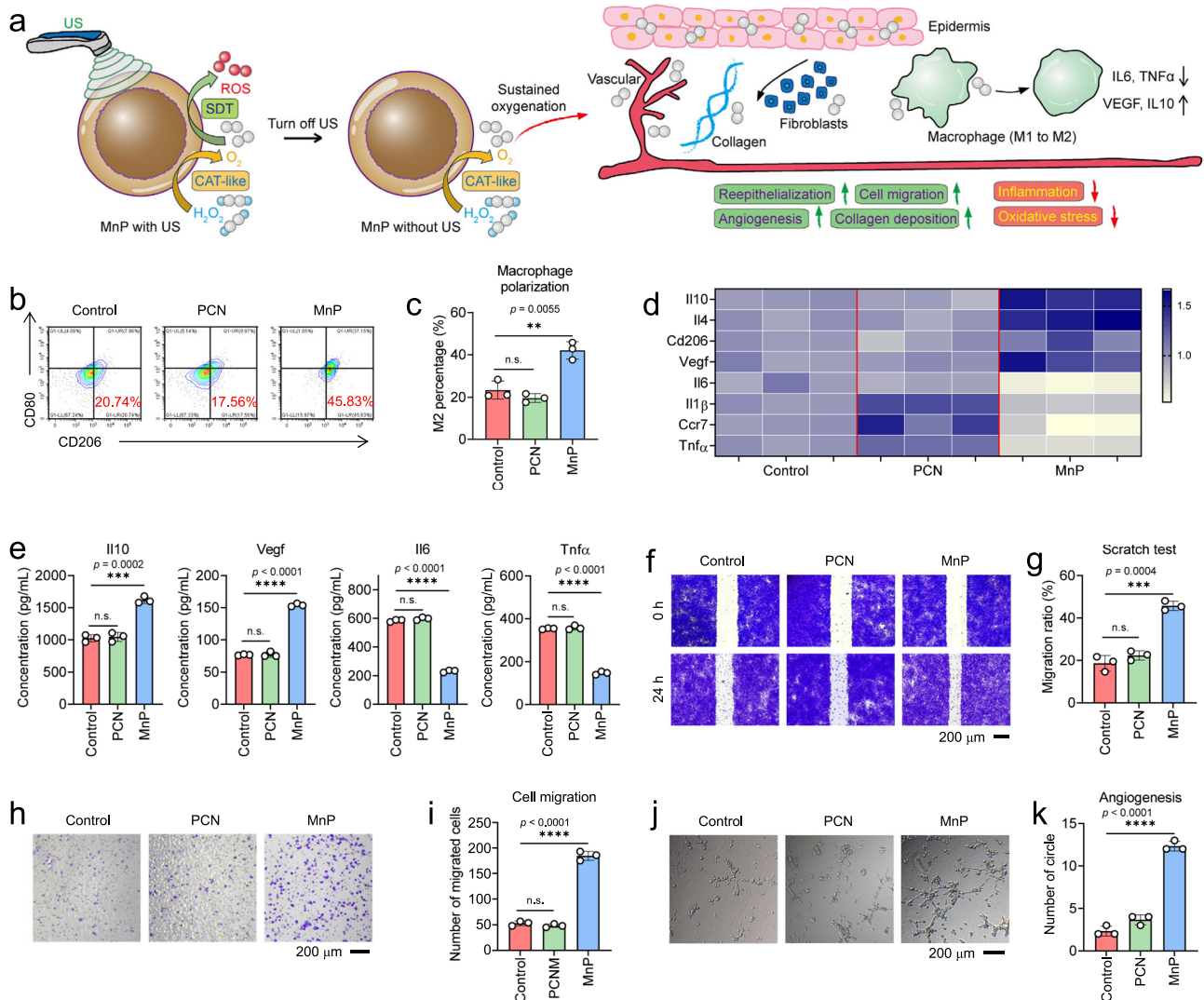


Fig. 8 | In vitro pro-tissue repair evaluation. **a** Schematic of posttreatment with SMIT therapy. Sustained oxygenation from MnP without US accelerated wound healing. **b** Flow cytometry of CD80 and CD206 expression on macrophage after different treatments. **c** M2-phenotype macrophage percentage. $n = 3$ independent experiments; means \pm SDs. n.s., not significant; $*p < 0.05$, $**p < 0.01$, $***p < 0.001$, and $****p < 0.0001$ using two-tailed Student's t tests. **d** Relative gene expression of RAW264.7 cells after different treatments by qPCR analysis. **e** ELISA detection of Il10, Vegf, Il6, and Tnf α in RAW264.7 cells after different treatments. $n = 3$ independent experiments; means \pm SDs. n.s., not significant; $*p < 0.05$, $**p < 0.01$, $***p < 0.001$, and $****p < 0.0001$ using two-tailed Student's t tests. **f** Scratch assay of EA.hy926 cells cultured in macrophage-conditioned media for 0 and 24 h with quantitative analysis of the migration ratio (**g**). Scale bar, 200 μ m. $n = 3$

independent experiments; means \pm SDs. n.s., not significant; $*p < 0.05$, $**p < 0.01$, $***p < 0.001$, and $****p < 0.0001$ using two-tailed Student's t tests. **h** Transwell migration assay of EA.hy926 cells in different groups with quantitative analysis of the number of migrated cells (**i**). Scale bar, 200 μ m. $n = 3$ independent experiments; means \pm SDs. n.s., not significant; $*p < 0.05$, $**p < 0.01$, $***p < 0.001$, and $****p < 0.0001$ using two-tailed Student's t tests. **j** Vascular tube formation of EA.hy926 cells cultured in various macrophage-conditioned media on Matrigel for 6 h with quantitative analysis of the number of circles (**k**). Scale bar, 200 μ m. $n = 3$ independent experiments; means \pm SDs. n.s., not significant; $*p < 0.05$, $**p < 0.01$, $***p < 0.001$, and $****p < 0.0001$ using two-tailed Student's t tests. Source data are provided as a Source Data file.

solution of *N,N*-dimethylformamide (DMF)/ethanol (EtOH). Then, 27.8 mg of zirconium chloride (ZrCl₄, Aladdin, China) and 50 mg of tetrakis(4-carboxyphenyl)porphyrin (TCPP, TCI, Shanghai) were added into the above mixed solution. After sonication in an ice bath for 10 min in the dark, the mixed solution was stirred at 90 °C for 6 h. Then, MnP products were collected by centrifugation, washed three times with ethanol, and freeze-dried for further use.

TEM (JEOL, JEM-2100 Plus, Japan) was used to observe the morphology of the nanoparticles. Elemental mapping was used to analyze the elemental composition of the materials. To evaluate oxygen generation, a dissolved oxygen meter (JPB-607A, INESA, Shanghai) was used to detect the generated oxygen gas in the DI water. ¹O₂ generation was detected by SOSG assay via fluorescence spectrometry.

To prepare MnPM, a neutrophil and macrophage hybrid membrane was used to encapsulate MnP nanoparticles. Herein, RAW264.7 cells were cultured in complete DMEM containing 10% fetal bovine serum. RAW264.7 cells (2×10^7 cells per well) were precipitated by centrifugation and resuspended in a precooled hypotonic buffer of 1 \times protease inhibitor (pH 7.4, 10 mM Tris, 1 mM MgCl₂) in an ice bath for half an hour. Similarly, neutrophils were isolated from the bone marrow of male mice (6–8 weeks). Frozen cells were thawed and washed three times with 1 \times PBS. Cells were then suspended in hypotonic buffer containing 30 mM Tris-HCl (pH 7.5, Sigma, T8230) and precooled 1 \times protease inhibitor (pH 7.4, 10 mM Tris, 1 mM MgCl₂) in an ice bath for half an hour. The disintegrated cells were centrifuged (1100 g, 4 °C, 15 min), and the supernatant was collected. The precipitate obtained

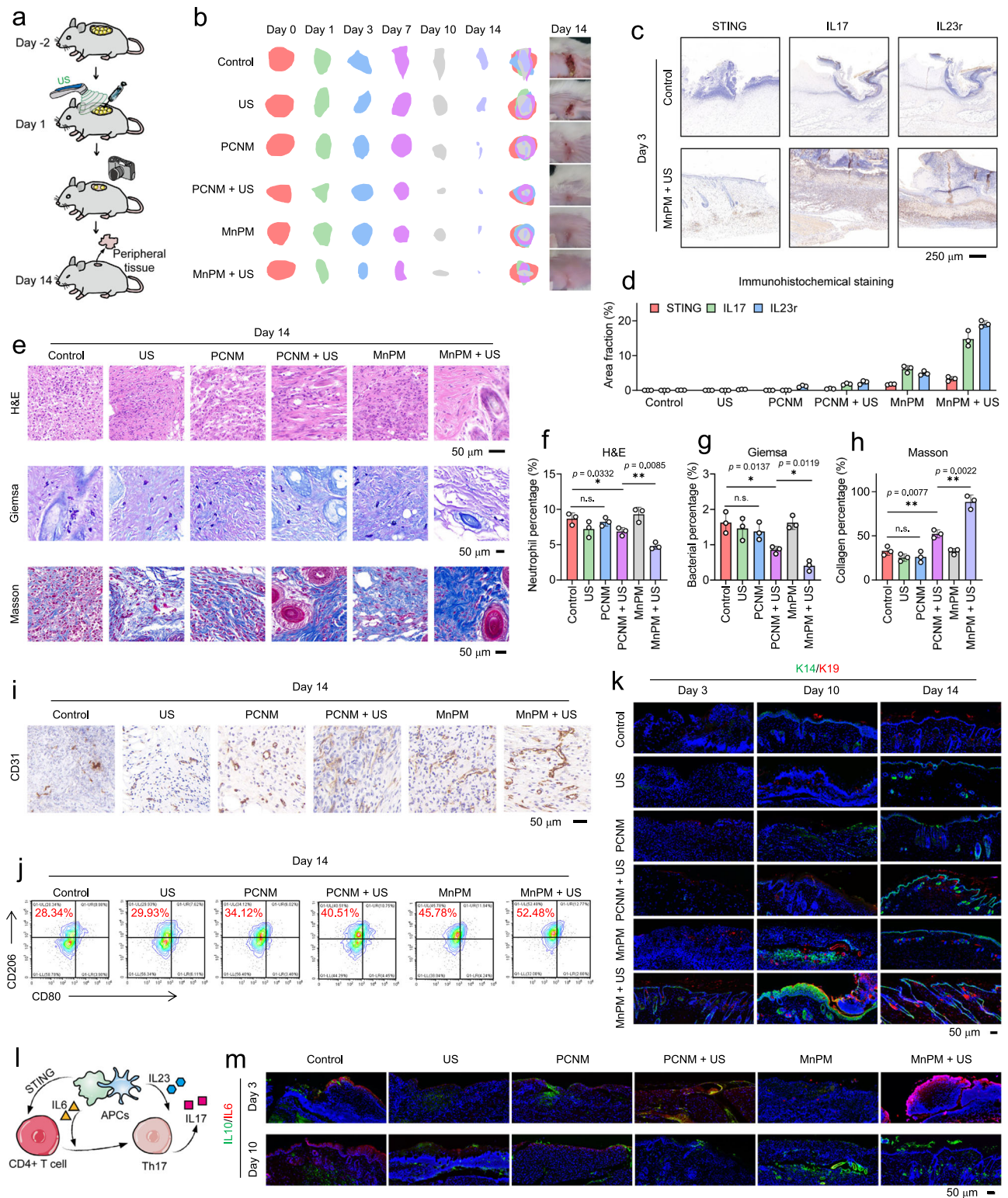


Fig. 9 | In vivo healing of infected skin wounds. **a** Schematic illustration of the experimental animal models of wound MRSA infection to evaluate SMIT and oxygen-mediated tissue repair. **b** Representative images of wound size changes during 14 days post-wounding. Immunohistochemical analysis. Immunohistochemical staining (**c**) with quantitative analysis (**d**) for STING, IL17, and IL23r on day 3. Scale bars, 250 μ m. $n = 3$ independent animals; means \pm SDs. n.s., not significant; * $p < 0.05$, ** $p < 0.01$, *** $p < 0.001$, and **** $p < 0.0001$ using two-tailed Student's t tests. **e–h** Histomorphological analysis via hematoxylin and eosin (H&E), Giemsa, and Masson's trichrome staining of the peripheral tissues after various treatments

with quantitative analysis (**f–h**). Scale bars, 50 μ m. $n = 3$ independent animals; means \pm SDs. n.s., not significant; * $p < 0.05$, ** $p < 0.01$, *** $p < 0.001$, and **** $p < 0.0001$ using two-tailed Student's t tests. **i** Immunohistochemical staining of CD31. Scale bars, 50 μ m. **j** M2-phenotype macrophages (CD80-CD206+) by gating on CD11b + F4/80+ cells. **k** Immunofluorescence staining of cytokeratin 14 (K14, green) and cytokeratin 19 (K19, red) for the wounds on days 3, 10, and 14. Scale bars, 50 μ m. **l** A scheme illustrating Th17 cell differentiation. **m** Immunofluorescence staining of IL10 (green) and IL6 (red) for the wounds on days 3 and 10. Scale bars, 50 μ m. Source data are provided as a Source Data file.

by centrifugation (100000 g, 4 °C, 120 min) of the collected supernatant was the cell membrane. After washing with 0.2 mM EDTA (100000 g, 4 °C, 60 min), the neutrophil and macrophage membranes were collected and stored at 4 °C for future use and at -80 °C for long-term storage. Finally, the extracted macrophage membrane dispersion (1 mg/mL), neutrophil membrane dispersion (1 mg/mL) and MnP nanoparticles (1 mg/mL) were mixed in DI water. The mixture was sonicated for 10 min and stirred at 800 rpm for 30 min. The mixture was then extruded sequentially through 400 nm and 200 nm polycarbonate porous membranes more than 20 times repeatedly using an Avanti microextruder. The free membranes were then removed by centrifugation (16060 g, 4 °C, 30 min) to further purify the obtained hybrid membrane-encapsulated MnP nanoparticles, noted as MnPM. The PKH67 Green Fluorescent Cell Linker Mini Kit and DiI (DiI18(3)) were used for fluorescence imaging of neutrophil and macrophage hybridization membranes.

Investigation of the in vitro antibiofilm mechanism

qPCR was performed to determine the relative expression levels of typical genes in three replicates using SYBR Green qPCR Master Mix (EZBioscience) and the QuantStudio 7 Flex system (Life Technologies). Gene expression levels were evaluated using the $2^{-\Delta\Delta Ct}$ method. The sequences of primers used for gene amplification were shown in Table S1. Elemental mapping was performed to determine the Mn ion content within the bacteria. The concentrations of protein leaked from the bacteria were determined using a BCA protein assay kit (Elabscience, China). ONPG hydrolysis was used to evaluate the membrane permeability of bacteria in the biofilm. The collected bacteria were incubated with ONPG solution (Yeasen, China). The absorbance at 420 nm of the mixed solution was recorded using an enzyme-labeled instrument (BioTek Epoch, USA). ROS (1O_2) within the bacteria were detected by a 2',7'-dichlorodihydrofluorescein diacetate (DCFH-DA) assay using a Reactive Oxygen Species Assay Kit (Beyotime, China). In this assay, 500 μ L of MRSA suspension (1×10^6 CFU/mL) was seeded into 24-well plates at 37 °C and incubated for 24 h. After different treatments, the biofilms were collected and resuspended in PBS and washed twice with PBS for coinubation with 10 μ M of DCFH-DA.

In vitro cGAS-STING evaluation

For Western blot analysis, cells were seeded in six-well plates and treated according to the different groups. Total protein from each group was extracted by RIPA lysis buffer, and the concentration was determined by a BCA protein quantification kit. Different molecular weight proteins were separated by SDS-PAGE gel electrophoresis, and then the protein bands were transferred to PVDF membranes. The membrane was blocked at room temperature for 1 h, washed 3 times with TBST for 5 min each time, incubated overnight at 4 °C with primary antibody against the target protein, washed 3 times with TBST, incubated at 4 °C for 2 h with horseradish peroxidase enzyme-labeled secondary antibody, washed 3 times with TBST, and developed by an ECL chemiluminescence reagent kit. The western blot antibodies used in this study were shown in Table S2.

The ELISA was performed by incubating cells with materials for 24 h, collecting the media, and centrifuging (2380 g, 30 min) to obtain the supernatants. Then, ELISA kits were used to determine cytokine concentrations in different collected supernatants.

In vivo antibiofilm and immune response analysis

The mouse implant-related biofilm infection model was established using BALB/c mice purchased from the School of Agriculture and Biology, Shanghai Jiao Tong University. The infection model mice were divided into 6 groups and subjected to different treatments as follows: Control, US, PCNM, PCNM+US, MnPM, and MnPM+US. The concentrations of both PCN and MnP used in the PCNM, PCNM+US, MnPM, and MnPM+US groups were 30 μ g/mL. The US power,

frequency, duty cycle, and irradiation time were 1.5 W/cm², 1 MHz, 50%, and 8 min, respectively. Herein, 200 μ L of MRSA bacterial suspension (1×10^7 CFU/mL) was cocultured with poly(ether-ether-ketone) (titanium disc, diameter = 8 mm, thickness = 0.5 mm) discs at 37 °C with 5% CO₂ for 48 h. Prior to biofilm implantation, 1% pentobarbital sodium was injected for intraperitoneal anesthesia, and the prefabricated titanium discs with biofilms were implanted subcutaneously at the back of the neck. After shaving, disinfection, incision, and implantation, the skin wounds were immediately sutured. On day 0, the implantation sites were subjected to various treatments. On days 0, 1, 3, 7, 10, and 14 after injection, photographs of the infected area were taken.

For in vivo flow cytometry analysis. Localized skin tissue or spleen was taken, rinsed with PBS and placed in 1 ml of 1640 medium containing digestive enzymes (1 mg/mL collagenase type I, 250 μ g/mL collagenase type II, 50 μ g/mL DNase I). These tissues were minced, digested for 45 min at 37 °C, filtered through a 40 μ m cell sieve, and centrifuged at 400 \times g for 3 min. Afterwards, 2 mL of erythrocyte lysate was added, lysed for 3 min and centrifuged, and the cells were washed by centrifugation with PBS. Then, CD16/32 blocking antibody was added, the cells were resuspended and placed on ice for 30 min for blocking, and the cells were washed by centrifugation with PBS. Subsequently, fluorescein-labeled antibody was added and incubated on ice for 30 min, and the cells were washed by centrifugation with PBS. Collected cells were resuspended in 500 μ L of PBS for flow cytometry. The flow antibodies used in this study were shown in Table S3.

In vivo bioluminescence imaging

The mouse implant-related biofilm infection model was established. Cy5.5-labeled MnP and MnPM nanoparticles were intravenously injected at the infected area. Then, an animal live imaging system (VISQUE InVivo Elite) was used to track diffusion and enrichment of nanoparticles in vivo.

In vivo antibiofilm and tissue repair analysis

The mouse wound infection model was prepared with BALB/c mice obtained from the School of Agriculture and Biology, Shanghai Jiao Tong University. Mice were anesthetized with pentobarbital sodium (1%), and the skin on the back was shaved and disinfected. Dorsal skin wounds 8 mm in diameter were made in the mice and 100 μ L MRSA solution (1×10^6 CFU/mL) was injected into tissues, which were then subjected to various treatments: Control, US, PCNM, PCNM+US, MnPM, and MnPM+US. The US power, frequency, duty cycle, and irradiation time were 1.5 W/cm², 1 MHz, 50%, and 8 min, respectively. Wounds in each group were photographed and recorded until euthanasia on days 0, 1, 3, 7, 10, and 14. On day 14, wound tissues were collected and fixed with paraformaldehyde (4%). The fixed tissues were then dehydrated in ethanol, embedded in paraffin, and sectioned for histological analysis. Hematoxylin and eosin (H&E) and Giemsa staining methods were used to evaluate inflammation and bacterial residue. All slides were viewed under an optical microscope (OLYMPUS, IX70, Japan). ImageJ/Fiji software (<https://imagej.nih.gov/ij/>) was used to quantify the data from three different images. All images were converted to binary with a fixed threshold to allow comparison of substrates. Images of immunohistochemical staining for CD31, IL17, IL23r, and STING were captured via microscopy (Ci-s, Nikon). Immunofluorescence co-staining images of K14/K19 and IL6/IL10 were observed under a fluorescence microscope (OLYMPUS, IX70, Japan). Histological observation of major organs (heart, liver, spleen, lung, and kidney) in different treatments was performed by H&E staining to evaluate the biosafety of these treatments.

Statistics and reproducibility

All data are presented as the means \pm SDs deviation from at least three parallel experiments. Statistical analysis between two groups was

performed by using two-tailed Student's *t* test. $P < 0.05$ was considered to be statistically significant.

Reporting summary

Further information on research design is available in the Nature Portfolio Reporting Summary linked to this article.

Data availability

The RNA-Seq data generated in this study have been deposited in the NCBI Gene Expression Omnibus database under the accession code GSE260971. The experimental data generated in this study are available within the Article and Supplementary Information. All other data are available from the corresponding authors upon request. Source data are provided with this paper.

References

1. Patel, R. Periprosthetic Joint Infection. *New Engl. J. Med.* **388**, 251–262 (2023).
2. Levy, S. B. & Marshall, B. Antibacterial resistance worldwide: causes, challenges and responses. *Nat. Med.* **10**, S122–S129 (2004).
3. Willyard, C. The drug-resistant bacteria that pose the greatest health threats. *Nature News* **543**, 15 (2017).
4. Arciola, C. R., Campoccia, D. & Montanaro, L. Implant infections: adhesion, biofilm formation and immune evasion. *Nat. Rev. Microbiol.* **16**, 397–409 (2018).
5. Flemming, H.-C. et al. Biofilms: an emergent form of bacterial life. *Nat. Rev. Microbiol.* **14**, 563–575 (2016).
6. Rumbaugh, K. P. & Sauer, K. Biofilm dispersion. *Nat. Rev. Microbiol.* **18**, 571–586 (2020).
7. Stewart, P. S. & Bjarnsholt, T. Risk factors for chronic biofilm-related infection associated with implanted medical devices. *Clin. Microbiol. Infect.* **26**, 1034–1038 (2020).
8. Kalelkar, P. P., Riddick, M. & García, A. J. Biomaterial-based antimicrobial therapies for the treatment of bacterial infections. *Nat. Rev. Mater.* **7**, 39–54 (2022).
9. Yang, C. et al. Inorganic nanosheets facilitate humoral immunity against medical implant infections by modulating immune co-stimulatory pathways. *Nat. Commu.* **13**, 4866 (2022).
10. Luzuriaga, M. A. et al. Metal–Organic Framework Encapsulated Whole-Cell Vaccines Enhance Humoral Immunity against Bacterial Infection. *ACS Nano* **15**, 17426–17438 (2021).
11. Tang, H. et al. Photosensitizer Nanodot Eliciting Immunogenicity for Photo-Immunologic Therapy of Postoperative Methicillin-Resistant *Staphylococcus aureus* Infection and Secondary Recurrence. *Adv. Mater.* **32**, 2107300 (2022).
12. Rosenberger, C. M. & Finlay, B. B. Phagocyte sabotage: disruption of macrophage signalling by bacterial pathogens. *Nat. Rev. Mol. Cell Bio.* **4**, 385–396 (2003).
13. Finlay, B. B. & McFadden, G. Anti-Immunology: Evasion of the Host Immune System by Bacterial and Viral Pathogens. *Cell* **124**, 767–782 (2006).
14. Frei, A. et al. Metals to combat antimicrobial resistance. *Nat. Rev. Chem.* **7**, 202–224 (2023).
15. Zhang, L. et al. A Peritumorally Injected Immunomodulating Adjuvant Elicits Robust and Safe Metalloimmunotherapy against Solid Tumors. *Adv. Mater.* **34**, 2206915 (2022).
16. Sun, X. et al. Amplifying STING activation by cyclic dinucleotide–manganese particles for local and systemic cancer metalloimmunotherapy. *Nat. Nanotechnol.* **16**, 1260–1270 (2021).
17. Chandrangsu, P., Rensing, C. & Helmman, J. D. Metal homeostasis and resistance in bacteria. *Nat. Rev. Microbiol.* **15**, 338–350 (2017).
18. Price, E. E. & Boyd, J. M. Genetic Regulation of Metal Ion Homeostasis in *Staphylococcus aureus*. *Trends Microbiol.* **28**, 821–831 (2020).
19. Ong, C. L. et al. An Antimicrobial Role for Zinc in Innate Immune Defense Against Group A *Streptococcus*. *J. Infect. Dis.* **209**, 1500–1508 (2014).
20. Shen, X. et al. Nano-decocted ferrous polysulfide coordinates ferroptosis-like death in bacteria for anti-infection therapy. *Nano Today* **35**, 100981 (2020).
21. Zhu, W. et al. Photothermal Nanozyme-based Microneedle Patch against Refractory Bacterial Biofilm Infection via Iron-actuated Janus Ion Therapy. *Adv. Mater.* **34**, 2207961 (2022).
22. Solórzano, P. K. P. et al. A Manganese-independent Aldolase Enables *Staphylococcus aureus* To Resist Host-imposed Metal Starvation. *mBio* **14**, e03223–22 (2023).
23. Grunenwald, C. M. et al. Manganese Detoxification by MntE Is Critical for Resistance to Oxidative Stress and Virulence of *Staphylococcus aureus*. *mBio* **10**, e02915–e02918 (2019).
24. García, Y. M. et al. A Superoxide Dismutase Capable of Functioning with Iron or Manganese Promotes the Resistance of *Staphylococcus aureus* to Calprotectin and Nutritional Immunity. *PLoS Path* **13**, e1006125 (2017).
25. Chaigne-Delalande, B. & Lenardo, M. J. Divalent cation signaling in immune cells. *Trends Immunol.* **35**, 332–344 (2014).
26. Hood, M. I. & Skaar, E. P. Nutritional immunity: transition metals at the pathogen–host interface. *Nat. Rev. Microbiol.* **10**, 525–537 (2012).
27. Bessman, N. J. et al. Dendritic cell-derived hepcidin sequesters iron from the microbiota to promote mucosal healing. *Science* **368**, 186–189 (2020).
28. Du, M. & Chen, Z. J. DNA-induced liquid phase condensation of cGAS activates innate immune signaling. *Science* **361**, 704–709 (2018).
29. Wang, C. et al. Manganese Increases the Sensitivity of the cGAS-STING Pathway for Double-Stranded DNA and Is Required for the Host Defense against DNA Viruses. *Immunity* **48**, 675–687.e7 (2018).
30. Kwon, J. & Bakhom, S. F. The Cytosolic DNA-Sensing cGAS–STING Pathway in Cancer. *Cancer Discov* **10**, 26–39 (2020).
31. Zhao, Z. et al. Tumor Microenvironment-Activable Manganese-Boosted Catalytic Immunotherapy Combined with PD-1 Checkpoint Blockade. *ACS Nano* **16**, 20400–20418 (2022).
32. Deng, Z. et al. Biomaterialized MnO₂ Nanoparticles Mediated Delivery of Immune Checkpoint Inhibitors with STING Pathway Activation to Potentiate Cancer Radio-Immunotherapy. *ACS Nano* **17**, 4495–4506 (2023).
33. Yan, J. et al. Engineering Radiosensitizer-Based Metal-Phenolic Networks Potentiate STING Pathway Activation for Advanced Radiotherapy. *Adv. Mater.* **34**, 2105783 (2022).
34. Gao, Z.-L. et al. Orchestrated Cytosolic Delivery of Antigen and Adjuvant by Manganese Ion-Coordinated Nanovaccine for Enhanced Cancer Immunotherapy. *Nano Lett* **23**, 1904–1913 (2023).
35. Tang, S. et al. MnO₂-melittin nanoparticles serve as an effective anti-tumor immunotherapy by enhancing systemic immune response. *Biomaterials* **288**, 121706 (2022).
36. Song, W. et al. Activating Innate Immunity by a STING Signal Amplifier for Local and Systemic Immunotherapy. *ACS Nano* **16**, 15977–15993 (2022).
37. Landman, S. L., Rensing, M. E. & van der Veen, A. G. Balancing STING in antimicrobial defense and autoinflammation. *Cytokine Growth Factor Rev* **55**, 1–14 (2020).
38. Horcajada, P. et al. Porous metal–organic-framework nanoscale carriers as a potential platform for drug delivery and imaging. *Nat. Mater.* **9**, 172–178 (2010).
39. Mendes, R. F. et al. Metal–organic frameworks: a future toolbox for biomedicine? *Chem. Soc. Rev.* **49**, 9121–9153 (2020).
40. Su, Z. et al. Bioresponsive nano-antibacterials for H₂S-sensitized hyperthermia and immunomodulation against refractory implant-related infections. *Sci. Adv.* **8**, eabn1701 (2022).

41. Su, Z. et al. Enzymatic bionanocatalysts for combating peri-implant biofilm infections by specific heat-amplified chemodynamic therapy and innate immunomodulation. *Drug Resistance Updates* **67**, 100917 (2023).
42. Wang, Z. et al. Recent advances in porphyrin-based MOFs for cancer therapy and diagnosis therapy. *Coord. Chem. Rev.* **439**, 213945 (2021).
43. Zhuang, F. et al. Sequential Ultrasound-Triggered and Hypoxia-Sensitive Nanoprodrug for Cascade Amplification of Sonochemotherapy. *ACS Nano* **16**, 5439–5453 (2022).
44. Li, S.-Y. et al. Cancer Cell Membrane Camouflaged Cascade Bioreactor for Cancer Targeted Starvation and Photodynamic Therapy. *ACS Nano* **11**, 7006–7018 (2017).
45. Zhang, W. et al. Enhanced Photodynamic Therapy by Reduced Levels of Intracellular Glutathione Obtained By Employing a Nano-MOF with Cull as the Active Center. *Angew. Chem. Int. Ed.* **57**, 4891–4896 (2018).
46. Zhang, L. et al. Porphyrinic Zirconium Metal–Organic Frameworks (MOFs) as Heterogeneous Photocatalysts for PET-RAFT Polymerization and Stereolithography. *Angew. Chem. Int. Ed.* **60**, 5489–5496 (2021).
47. Luo, Z. et al. Light-Induced Redox-Responsive Smart Drug Delivery System by Using Selenium-Containing Polymer@MOF Shell/Core Nanocomposite. *Adv. Healthc. Mater.* **8**, 1900406 (2019).
48. Oh, J. Y. et al. Protein-Precoated Surface of Metal–Organic Framework Nanoparticles for Targeted Delivery. *Small* **19**, 2300218 (2023).
49. Liu, Y. et al. Ostwald Ripening-Mediated Grafting of Metal–Organic Frameworks on a Single Colloidal Nanocrystal to Form Uniform and Controllable MXF. *J. Am. Chem. Soc.* **141**, 7407–7413 (2019).
50. Hu, J. et al. Fabrication of Glyco-Metal–Organic Frameworks for Targeted Interventional Photodynamic/Chemotherapy for Hepatocellular Carcinoma through Percutaneous Transperitoneal Puncture. *Adv. Funct. Mater.* **30**, 1910084 (2020).
51. Shao, Y. et al. Engineering of Upconverted Metal–Organic Frameworks for Near-Infrared Light-Triggered Combinational Photodynamic/Chemo-/Immunotherapy against Hypoxic Tumors. *J. Am. Chem. Soc.* **142**, 3939–3946 (2020).
52. Sun, Z. et al. Biodegradable MnO-Based Nanoparticles with Engineering Surface for Tumor Therapy: Simultaneous Fenton-Like Ion Delivery and Immune Activation. *ACS Nano* **16**, 11862–11875 (2022).
53. Nel, A. E. et al. Understanding biophysicochemical interactions at the nano–bio interface. *Nat. Mater.* **8**, 543–557 (2009).
54. Wang, W. et al. Engine-Trailer-Structured Nanotrucks for Efficient Nano-Bio Interactions and Bioimaging-Guided Drug Delivery. *Chem* **6**, 1097–1112 (2020).
55. Yang, K. et al. Role of manganese dioxide in the recovery of oxide–sulphide zinc ore. *J. Hazard. Mater.* **343**, 315–323 (2018).
56. Luo, Y. Preparation of MnO₂ nanoparticles by directly mixing potassium permanganate and polyelectrolyte aqueous solutions. *Mater. Lett.* **61**, 1893–1895 (2007).
57. Bachmann, M. F. & Jennings, G. T. Vaccine delivery: a matter of size, geometry, kinetics and molecular patterns. *Nat. Rev. Immunol.* **10**, 787–796 (2010).
58. Deng, R. et al. Intracellular Glutathione Detection Using MnO₂-Nanosheet-Modified Upconversion Nanoparticles. *J. Am. Chem. Soc.* **133**, 20168–20171 (2011).
59. Huang, D. et al. Bio-inspired temporospatial catalytic cascades systems based on ultrasound-triggered multicomponent piezoelectric microparticles. *Aggregate* **5**, e534 (2024).
60. Fang, R. H. et al. Cell Membrane Coating Nanotechnology. *Adv. Mater.* **30**, 1706759 (2018).
61. Kolaczowska, E. & Kubers, P. Neutrophil recruitment and function in health and inflammation. *Nat. Rev. Immunol.* **13**, 159–175 (2013).
62. Shi, C. & Pamer, E. G. Monocyte recruitment during infection and inflammation. *Nat. Rev. Immunol.* **11**, 762–774 (2011).
63. Naik, S. et al. Commensal–dendritic-cell interaction specifies a unique protective skin immune signature. *Nature* **520**, 104–108 (2015).
64. Korn, T. et al. IL-17 and Th17 Cells. *Annu. Rev. Immunol.* **27**, 485–517 (2009).
65. Decout, A. et al. The cGAS–STING pathway as a therapeutic target in inflammatory diseases. *Nat. Rev. Immunol.* **21**, 548–569 (2021).
66. An, J. et al. Enhancement of the viability of T cells electroporated with DNA via osmotic dampening of the DNA-sensing cGAS–STING pathway. *Nat. Biomed. Eng.* **8**, 149–164 (2024).
67. Mirchandani, A. S. et al. Hypoxia shapes the immune landscape in lung injury and promotes the persistence of inflammation. *Nat. Immunol.* **23**, 927–939 (2022).
68. Schreml, S. et al. Oxygen in acute and chronic wound healing. *Br. J. Dermatol.* **163**, 257–268 (2010).
69. Campisi, L. et al. Apoptosis in response to microbial infection induces autoreactive TH17 cells. *Nat. Immunol.* **17**, 1084–1092 (2016).
70. Michel, M. et al. Keratin 19 as a biochemical marker of skin stem cells in vivo and in vitro: Keratin 19 expressing cells are differentially localized in function of anatomic sites, and their number varies with donor age and culture stage. *J. Cell Sci.* **109**, 1017–1028 (1996).
71. Fradette, J. et al. The Type I Keratin 19 Possesses Distinct and Context-dependent Assembly Properties*. *J. Biol. Chem.* **273**, 35176–35184 (1998).

Acknowledgements

The authors would like to acknowledge the financial support from Funded by the National Natural Science Foundation of China (82102586 to Z.S., 82272512 to C.Z., 82302718 to L.K.), the Natural Science Foundation of Anhui Province, Distinguishing Youth Project (2108085J40 to C.Z.), Anhui Provincial Key Research and Development Program-Clinical Medical Research Translation Specialization (202304295107020020 to C.Z.), the Key Research and Development Plan of Jiangsu Province (BE2023844 to W.F.), the Funding of Double First-Rate Discipline Innovation Team of China Pharmaceutical University (CPUQJNC22_04 to W.F.), China Postdoctoral Science Foundation (2020M671893 to Z.S.), the Fundamental Research Funds for the Central Universities of China (WK9110000155 to Z.S., 2632023TD01 to W.F.), Anhui Provincial Scientific Research Compilation Project (2022AH051251 to Z.S., 2022AH010076 to C.Z.), Research Funds of Centre for Leading Medicine and Advanced Technologies of IHM (2023IHM01070 to C.Z., 2023IHM01074 to C.Z.). We also thank for the support from the Core Facility Center for Medical Sciences, The First Affiliated Hospital of USTC (Anhui Provincial Hospital). This work was partially carried out at the Instruments Center for Physical Science, University of Science and Technology of China. We acknowledge the Public Platform of State Key Laboratory of Natural Medicines for the use of analytical instrumentation facilities (FUJIFILM VisualSonics Vevo LAZR) and also thank Li Guo and Yingjie Xu for their assistance of taking images.

Author contributions

Z.S., W.Z., W.F., and C.Z. conceived and designed the concept of the experiments. Z.S., X.H. and W.F. synthesized the materials. Z.S., Z.Q., X.H., and W.F. conducted the material characterizations. Z.S., D.X., L.K., X.H., J.M., R.M., and W.Z. conducted and analyzed most of the in vitro and in vivo experiments. Z.S. wrote the manuscript. Z.S., D.X., X.H., W.Z., W.F., X.S., and C.Z. provided important experimental insights and cowrote the paper. All authors discussed, commented, and agreed on the manuscript.

Competing interests

The authors declare the following competing interests: Z.S., C.Z., W.Z., D.X., and X.H. are inventors on a patent application (China Patent No. CN117018025A) based on the technology presented in this manuscript. The others authors declare no competing interests.

Additional information

Supplementary information The online version contains supplementary material available at <https://doi.org/10.1038/s41467-024-52489-x>.

Correspondence and requests for materials should be addressed to Zheng Su, Wanbo Zhu, Wenpei Fan or Chen Zhu.

Peer review information *Nature Communications* thanks Lizeng Gao, and the other, anonymous, reviewer(s) for their contribution to the peer review of this work. A peer review file is available.

Reprints and permissions information is available at <http://www.nature.com/reprints>

Publisher's note Springer Nature remains neutral with regard to jurisdictional claims in published maps and institutional affiliations.

Open Access This article is licensed under a Creative Commons Attribution-NonCommercial-NoDerivatives 4.0 International License, which permits any non-commercial use, sharing, distribution and reproduction in any medium or format, as long as you give appropriate credit to the original author(s) and the source, provide a link to the Creative Commons licence, and indicate if you modified the licensed material. You do not have permission under this licence to share adapted material derived from this article or parts of it. The images or other third party material in this article are included in the article's Creative Commons licence, unless indicated otherwise in a credit line to the material. If material is not included in the article's Creative Commons licence and your intended use is not permitted by statutory regulation or exceeds the permitted use, you will need to obtain permission directly from the copyright holder. To view a copy of this licence, visit <http://creativecommons.org/licenses/by-nc-nd/4.0/>.

© The Author(s) 2024

¹Department of Orthopedics, Centre for Leading Medicine and Advanced Technologies of IHM, The First Affiliated Hospital of USTC, Division of Life Sciences and Medicine, University of Science and Technology of China, Hefei, Anhui 230001, China. ²Department of Orthopedics, The First Affiliated Hospital of Zhengzhou University, Zhengzhou 450000, PR China. ³Department of Orthopaedics, Shanghai Sixth People's Hospital Affiliated to Shanghai Jiao Tong University School of Medicine, Shanghai Jiao Tong University, Shanghai 200233, PR China. ⁴Department of Orthopedics, Changhai Hospital of Shanghai, Shanghai 200433, China. ⁵State Key Laboratory of Natural Medicines and Jiangsu Key Laboratory of Drug Discovery for Metabolic Diseases, Center of Advanced Pharmaceuticals and Biomaterials, China Pharmaceutical University, Nanjing 211198, China. ⁶These authors contributed equally: Zheng Su, Dongdong Xu, Xianli Hu. ✉ e-mail: suz924@ustc.edu.cn; zhuwanbo@sjtu.edu.cn; wenpei.fan@cpu.edu.cn; zhuchena@ustc.edu.cn